Facultad
de
Ciencias

Obtention of bulk $SrTiO_3$ phase diagrams as a function of strain and temperature

(Obtención de los diagramas de fase del $SrTiO_3$ en volumen como función de la tensión y la temperatura)

Trabajo de Fin de Grado
para acceder al

GRADO EN FÍSICA

Autor: Raúl Coterillo Ruisánchez
Director: Francisco Javier Junquera Quintana

Julio - 2020

A mis padres, Rodolfo y Almudena,
por darme la educación que
ellos nunca pudieron tener,
y a Beatriz, a quien quiero
como a una hermana.

The most important step a man can take.
It's not the first one, is it? It's the next one.
Always the next step, Dalinar.

-Brandon Sanderson, "*Oathbringer*"

AGRADECIMIENTOS

En primer lugar me gustaría dar las gracias a Javier, mi director en este trabajo, tanto por haber confiado en mí en un primer momento como por su constancia y dedicación a lo largo del proyecto, a pesar de las desafortunadas dificultades técnicas derivadas de la pandemia. Asimismo, me gustaría agradecer a Pablo su ayuda con los entresijos de Fortran; a las Nats, por enseñarme todo el inglés que sé; y a Carmen, por redescubrirme a tiempo el mundo de las matemáticas.

Querría dedicar también unas líneas a mis compañeros de facultad, quienes increíblemente han conseguido aguantarme durante todos estos años: A Viti, Pablo, las Meris, Marta, Revu, Rubenuco, Carmen, Pau, Natillas, Sara, Lucía, Antonio, Mario, Irene, ... y más recientemente a Toñin y Mariela. Aunque nuestros caminos se separen, tened por cierto que siempre os llevaré conmigo.

Me gustaría a su vez recordar a todos aquellos que me acompañaron durante mi año en Milán, el cual ha sido sin duda una de las mejores experiencias de mi vida. En especial a Clara y a Jorge, ya que estoy completamente seguro de que sin vosotros no hubiese sido lo mismo.

Y aunque no os pueda mencionar a todos, no podría haber haber llegado a ninguna parte sin toda esa gente maravillosa que me ha acompañado en este camino: Elena, Sergio, Toñin, Justo, Gerardo, Candela, Ángel, Satu, Diego, Rubén, Carlos, ... La verdad que os merecéis un premio por escuchar todas mis retahílas, tanto de física como de la vida en general.

Finalmente quiero agradecer a mi familia su apoyo incondicional, que siempre me ha permitido dedicarme a lo que me apasiona. Si estoy aquí es gracias a vosotros, y a la educación que me habeis dado tanto en el sentido académico como en el personal. Como tanto os gusta decir: "*Lo bien hecho, bien parece.*"

A Lula, Nika, Pipo y Kira.
Gracias por tanto.

Abstract

Strontium titanate ($SrTiO_3$) is one of the most widely used substrates when it comes to epitaxial growth of functional oxide thin films. It has been an attractive subject of research mainly due to its incipient ferroelectric behavior at low temperatures.

At room temperature, and under standard conditions it exhibits a cubic phase ($Pm\bar{3}m$) perovskite structure. However when temperature drops below 105 K it undergoes an antiferrodistortive phase transition due to the rotation of the oxygen octahedra, shifting to a tetragonal (I4/mcm) phase in the process. At really low temperatures ($\sim$4 K) a ferroelectric transition should take place, were it not obstructed by quantum fluctuations (a situation known as quantum paraelectricity). This ferroelectric transition may also be fostered by applying epitaxial strain (modifying its lattice constants) or electric fields.

Making use of Monte Carlo simulations from second principles an attempt will be made to replicate the aforementioned antiferrodistortive transition, as well as to observe the material's temperature-dependant behaviour while imposing strain restrictions, enabling the obtention of a bulk $SrTiO_3$ phase diagram. This type of diagrams, known as Pertsev diagrams, are really sought after by experimental groups as they represent a trustworthy guide while navigating the different phases of the material at hand. This represents one of the most interesting aspects of this work, as this kind of diagrams have never been published while being produced with atomistic simulations (they are only accessible via phenomenological Ginzburg-Landau models).

This novelty is mainly due to the large size of the simulations involved -between 2500 and 5000 atoms-, only possible thanks to the second-principles techniques used in this work. They provide a much greater efficiency compared to traditional DFT methods while maintaining a similar level of precision.

This has granted the opportunity to carry out an analysis of the domain structure within several phases of the material, some of which displaying interesting, unexpected patterns. The previously mentioned rotations as well as ferroelectricity-related distortions have been quantified by means of a generalized mode projection system, developed specifically for this work.

Keywords: Strontium titanate, second-principles simulation, Monte Carlo techniques, ferroelectricity, temperature-strain phase diagram, domains

Resumen

El titanato de estroncio ($SrTiO_3$) es uno de los materiales más utilizados como substrato para crecer de forma epitaxial láminas delgadas de óxidos funcionales. Se trata de un material ampliamente estudiado sobretodo debido a su comportamiente de ferroeléctrico incipiente a bajas temperaturas.

A temperature ambiente, y en condiciones estándar posee una estructura perovskita en fase cúbica ($Pm\bar{3}m$). Sin embargo al descender por debajo de los 105 K sufre una transición antiferrodistortiva debida a la rotación de los octaedros de oxígeno, pasando a una fase tetragonal (I4/mcm) en el proceso. A muy bajas temperaturas ($\sim$4 K) debería observarse una transición ferroeléctrica, pero está frustrada por las fluctuaciones cuánticas (se dice que es un paraeléctrico cuántico). Esta transición ferroeléctrica se puede activar a través otros mecanismos, como aplicando tensiones epitaxiales (modificaciones de su parámetro de red) o campos eléctricos.

Mediante simulaciones Monte Carlo desde segundos principios se tratará de replicar la transición antiferrodistortiva ya mencionada, así como observar su comportamiento con la temperatura al aplicar restricciones de tensión, permitiendo obtener un diagrama del fases de $SrTiO_3$ en volumen. Este tipo de diagramas, denominados diagramas de Pertsev, son muy codiciados por los grupos experimentales ya que suponen una guía fiable para navegar entre las diferentes fases que pudieran aparecer. Esto supone uno de los mayores puntos de interés de este trabajo, ya que este tipo de diagramas nunca se han publicado con simulaciones atómicas (solo son accesibles con modelos fenomenólogicos del tipo de Ginzburg-Landau).

Esta novedad se debe principalmente al gran tamaño de las simulaciones utilizadas -de entre 2500 y 5000 átomos-, posibles gracias al uso de técnicas de segundos principios, que permiten una mayor eficiencia que los métodos DFT tradicionales con una precisión similar.

Esto ha permitido, por ejemplo, un análisis de la estructura de dominios en diversas fases del material, llegándose a observar patrones relativamente complejos e inesperados. Tanto dichas rotaciones como las posibles distorsiones ferroeléctricas se han cuantificado por medio de un sistema generalizado de proyección de modos, desarrollado explícitamente para este trabajo.

Palabras clave: Titanato de estroncio, simulación de segundos principios, métodos Monte Carlo, ferroelectricidad, diagrama de fases temperatura-tensión, dominios

CONTENTS

CHAPTER 1

INTRODUCTION

I Motivation for this Work

I.i Ferroelectricity

Ferroelectric materials have been an important subject of study in the field of solid state physics over the last fifty years due to their wide range of properties and potential applications. Materials displaying ferroelectricity possess an spontaneous electric polarization which is reversible under the application of an external electric field, similarly to how ferromagnetic materials retain a permanent magnetic moment.

In fact the former were named directly due to their relation with the latter, as both phenomenons share a host of their most characteristic properties, namely the existence of hysteresis cycles (Fig.1.1) in the reversal of their respective properties and the fact that the materials which present them only do so below a certain temperature threshold, generally known as its Curie temperature (named so after Pierre Curie).

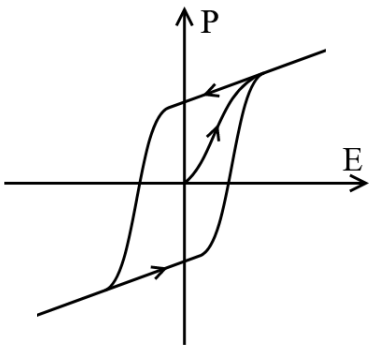

Figure 1.1: Depiction of a typical ferroelectrical hysteresis cycle.

Whereas their persistent polarization (and their high dielectric permitivity) render them useful for the development of smaller, tunable capacitors and faster, more energy-efficient computer memory [63], the fact that they also exhibit piezoelectric and pyroelectric behaviours (implied by sheer symmetry arguments regarding the nature of ferroelectricity) makes them suitable for a wide variety of sensing applications, from infrared, pressure or flow sensors to ultrasonic transducers for medical imaging [10]. They have also seen extensive use due to their catalytic properties, mainly a byproduct of the polarization-induced surface charges [13, 34]. Moreover, lots of research is being driven towards the development of multiferroic materials and heterostructures, which combine the strengths of both ferromagnetism and ferroelectricity unlocking interesting potential applications [58].

The main goal of this work lies in furthering the understanding of the driving mechanisms behind this interesting property by carrying out a computational study of strontium titanate ($SrTiO_3$), an edge-case within this class of materials. Although in its bulk state it seems to start undergoing a ferroelectric transition, its dielectric permitivity never diverges as it should in a normal ferroelectric, stabilizing instead as it reaches 4 K [51]. This anomalous behaviour, known as quantum paraelectricity, is explained in terms of the soft-mode theory of ferroelectricity [8] as the frequency of the soft-mode corresponding to the transition remaining stable (that is, never reaching zero) due the effects of quantum fluctuations [77].

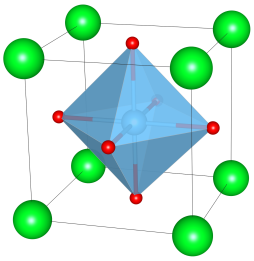

Figure 1.2: $SrTiO_3$ unit cell. Sr, Ti and O atoms are represented, respectively by green, blue and red spheres.

Nonetheless it has been shown both theoretically [56] and experimentally [25] that ferroelectricity can be attained by simply applying a misfit strain, a situation whose replication was attempted in the computer simulations carried out in this work. Electric field induced ferroelectricity has recently been recently reported [43], and could be simulated with the methods used here too. As a final note, isotopic substitution of oxygen-16 for oxygen-18 also seems to raise the temperature at which the permitivity stabilizes [30].

I.ii Strontium Titanate

Strontium titanate ($SrTiO_3$, herein refered to as STO) was first patented along with other titanates ($BaTiO_3$, $CaTiO_3$) in the 1940s and 1950s, and it was thought to be a completely artificial material until its natural counterpart, tausonite, was discovered in Siberia in 1982.

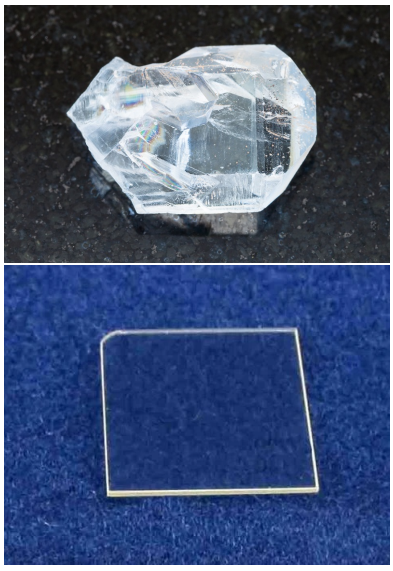

Figure 1.3: $SrTiO_3$ in unpolished (top) and substrate (bottom) form.

Synthetics are usually transparent and colorless (see Fig.1.3), although they can acquire different colours when doped by rare earth elements or transition metals. It is a brittle material which presents a refractive index of $n = 2.410$ ($\lambda = 589.3$ nm) and high dispersion, melting at relatively high temperatures (2350 K).

Under standard conditions STO presents a cubic ($Pm\bar{3}m$) perovskite structure, each titanium atom laying in the center of an oxygen octahedron with strontium filling the interstices (see Fig.1.2), but diverges from said aristotype [48] as it undergoes an antiferrodistortive phase transition comprising an out-of-phase rotation of the oxygen octahedra at 105 K which devolves into a tetragonal (I4/mcm) structure with its c axis pointing in the same direction as the octahedral axis of rotation. Decreasing the temperature even further results in the aforementioned display of quantum paraelectricity.

Beside its more straightforward uses as material for optical windows [42] or as a diamond simulant in jewellery during the second half of the previous century, its properties as an incipient ferroelectric plus a convenient lattice parameter (~ 3.9 Å) have made it an ideal choice as a substrate for growing other materials [38, 68], particularly perovskite oxides. One remarkable example is $LaAlO_3$ grown in STO, as the interface between both substances (both insulators) can exhibit metallic conductivity [53], superconductivity and ferromagnetism [2], amongst other properties which neither of them present individually. It has also seen usage in catalysis [55] and photo-catalysis [57] related applications.

Although a slight variation of the Verneuil's process is the most common option when it comes to synthesizing bulk STO, in its thin film form it can be grown epitaxially by atomic layer deposition [45] or via scanning tunneling microscopy. Synthesis of STO nanoparticles [76] and nanorods [71] for research in catalysis and nanoscale ferroelectricity has also been reported. For additional information on the synthesis, properties and uses of STO, refer to [70].

II Computer-based Experimentation

The end goal of this work revolves around the simulation of bulk STO at finite temperatures in order to observe the previously mentioned antiferrodistortive phase transitions under strain-free conditions, therefore partially replicating the results in [27].

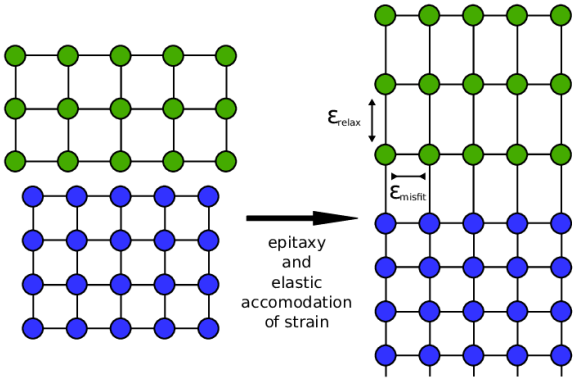

Figure 1.4: Effects of epitaxial strain in deposition layers. Image taken from Ref. [46].

Furthermore, by introducing in-plane strain constraints -both compressive and expansive- into said simulations we hope to produce a temperature-strain '*Pertsev*' phase diagram of bulk $SrTiO_3$, previously obtained only for thin films by means of Ginzburg-Landau-Devonshire theory [56].

Roughly speaking, Landau theory is a symmetry-based analysis of equilibrium behavior within a physical system near a phase transition [6], characterizing said transitions in terms of a series expansion the system's free energy $\mathcal{F}$ as a function of an order parameter and/or some external field.

The simulation of STO under in-plane strain is highly relevant due to its widespread use as an epitaxial growth substrate, as lattice mismatch between the substrate and the material to be grown (that is, a noticeable difference between their lattice parameters) generates epitaxial and relaxation strains (see Fig.1.4) that may lead to dislocations and imperfections in the resulting crystal. Moreover, control over STO's incipient ferroelectricity may be achieved by applying an epitaxial strain, rendering it useful for a wide variety of applications.

II.i Simulation Software

Computational material science has become a key research asset over the last few decades, as recent advances in computer speed and technology have allowed the creation of simulation techniques of ever-growing complexity, capable of exploring physical phenomena in scenarios where direct experimentation may prove too challenging and/or costly. Nonetheless, experimental results are still important in order to validate the predictions of computer models and simulations.

The main tool behind the simulations carried out in this work are second-principles techniques, specifically the SCALE-UP [16] implementation. This kind of simulations make use of models, whose parameters are obtained by means of first-principles or *ab initio* techniques, in order to replicate the accuracy of the latter with a substantial increase in calculation speed. This performance increase grants the ability to simulate larger systems (see Fig.1.5), in which size-related complex behaviours (such as domain structures) may arise.

Particularly, in this work we employ Monte Carlo techniques within the aforementioned second-principles framework[1] in order to explore the different phases of bulk STO at finite-temperatures. This was done under periodic boundary conditions and fixed-bond topology constraints within large ($8 \times 8 \times 8$ or $10 \times 10 \times 10$) supercells. A mode-projection Python algorithm (Appendix A) was devised in order to isolate and analyze the contributions from the different structural distortions (AFD^a, AFD^i, FE) present in bulk STO, therefore characterizing the different phases within the material.

III Objectives of this Bachelor Thesis

Having covered the most relevant aspects and motivations behind the present work, we may ask a few questions about our prospective goals:

- Can we reliably observe the antiferrodistortive phase transition present in STO?
- If so, are we able to replicate previous theoretical and experimental results?
- Can we produce a strain-temperature phase diagram of STO?
- Does said diagram replicate the results from Ginzburg-Landau theory? Do experimental results agree with either one of them?
- Can we observe any domain structures in our simulations?

These questions shall be answered within this thesis, following the structure outlined below:

Chapter 2 encloses a more in-depth description of the properties of strontium titanate exposed in this introduction, along with state-of-the-art explanations. In Chapter 3 a brief summary of modern first-principles simulation techniques, as well as the main ideas behind second-principles density functional theory will be presented.

In Chapter 4 the experimental methodology of simulating and interpreting the phase transitions studied in this work is explained, from the use of Monte Carlo techniques to the way in which phase transitions and structural modes were analyzed. Chapter 5 contains the main results of this work, concerning the antiferrodistortive phase transition and the temperature-strain phase diagram. Finally within Chapter 6 the main conclusions of this project will be summarized, altogether with some final remarks and suggestions for possible improvements and future research pathways.

[1] The model used in this work was created by J.C. Wojdeł et al. for [27] using the ABINIT [23] package

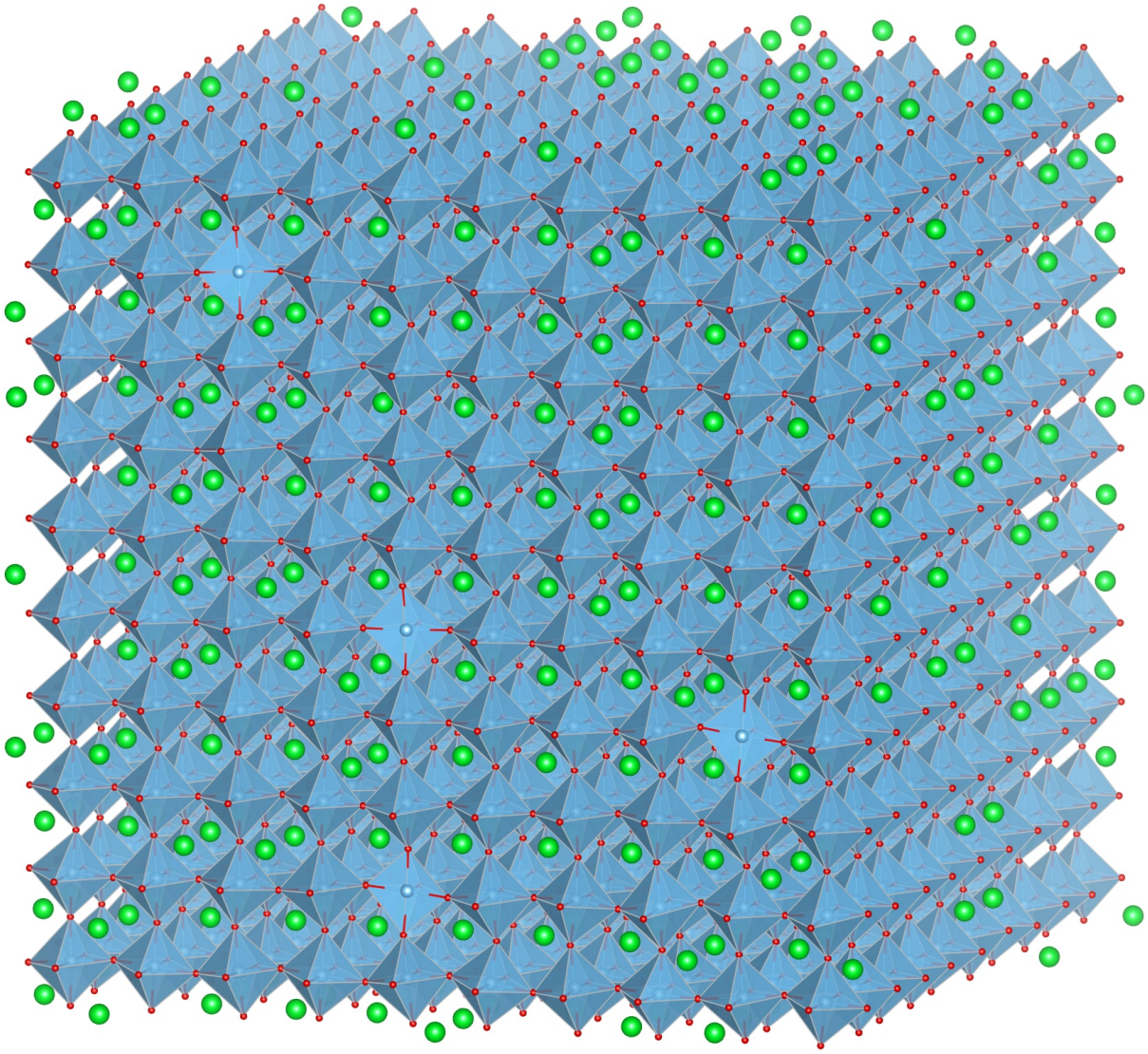

Figure 1.5: $10 \times 10 \times 10$ STO supercell, similar to the ones analyzed in this work. The strontium (green) atoms fill the interstices between the oxygen (red) octahedra, containing the titanium (blue) atoms. Image obtained using VESTA [50].

CHAPTER 2

THEORETICAL BACKGROUND

The following chapter aims to introduce the theory behind some of the most relevant properties of STO. First and foremost a description of the perovskite structure will be given, followed by some explanations on the origin of ferroelectricity and the structural phase transitions studied in this work.

I Perovskite Structure

The perovskite structure, typical of ABO_3 type oxides such as STO, takes its name from the homonymous mineral ($CaTiO_3$) where it was first observed.

The ideal perovskite structure, generally the high-temperature stable phase or *aristotype* [48], often undergoes structural distortions to more energetically stable, lower-symmetry phases in consequence to changes in different environmental factors such as temperature, pressure and/or strain. Fig. 1.2 shows the conventional unit cell used to represent this kind of compounds, while Fig. 2.1 is a rendition of its key component: the oxygen octahedra. Although cation displacement (generally the B site) is the main factor when it comes to the display of ferroelectric properties, the rotation of the octahedra within the cell (if present) is of utmost important in establishing the overall space-group symmetry of a given perovskite phase [19], usually differing from the $Pm\bar{3}m$ space-group presented by the aristotype. While atoms in the A site posses a 12-fold coordination, both the B site atoms and the oxygen atoms have a 6-fold coordination.

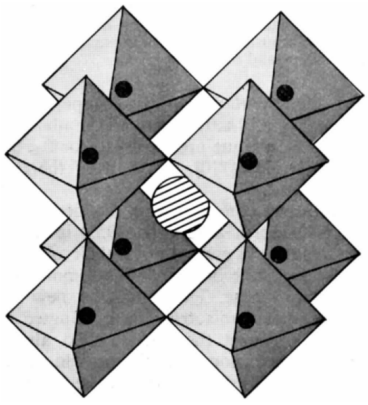

Figure 2.1: Depiction of the perovskite structure, showing the A cation (shaded) between eight oxygen octahedra containing the B cations (dark). Image taken from Ref. [48].

An array of several interesting properties, namely their high dielectric constant and absorption coefficient, as well as the display of ferroelectric (and therefore piezoelectric and piroelectric) properties, have made them ideal candidates for optoelectronic and photovoltaic applications [69], in addition to those mentioned in Chapter 1 regarding ferroelectric materials.

II Structural Phase Transitions

The aforementioned phase transitions in the perovskite structure are associated to atomic displacements diverging from the aristotype structure, known as modes. Those most relevant in the study of STO are the oxygen octahedra rotations, also known antiferrodistortive mode (henceforth referred to as AFD), and the displacement of the B cation inside the octahedra, known as the ferroelectric mode (FE, respectively) due to its relation with said property.

II.i Antiferrodistortive Mode

Although STO displays the aforementioned aristotypical cubic structure under standard conditions at temperatures higher than 105 K, other titanates such as $CaTiO_3$ present low-symmetry phases fostered by the presence of antiferrodistortive modes up to around 1600 K, meaning this kind of distortions are stable in a wide range of temperatures.

In 1972 Glazer introduced a classification system for the 23 possible different systems of octahedral rotations in perovskites, always under the assumption that the octahedra remain regular throughout [19]. Each system is represented by three letters representing the tilting magnitude along each direction ([100], [010], [001]), with equal letters meaning equal tilt, each accompanied by one symbol (+, - or 0) denoting, respectively, whether successive octahedra in the same axis posses an in-phase tilting (also referred to as AFD^i in this work), an anti-phase one (conversely AFD^a) or no tilting at all (see Fig. 2.4).

As reported by Chen [7] the most common system, displayed by around half perovskite oxides, is that of $GdFeO_3$ ($a^-a^-c^+$), with anti-phase rotations within the $x-y$ plane and in-phase rotations in the z direction, usually associated with orthorhombic structures. In the case of bulk STO the $a^0a^0c^-$ system is displayed below the 105 K phase transition, an anti-phase rotation of the octahedra along the z-axis (AFD^a_z) accompanied by a tetragonal structure elongated in that same direction. Several other systems are displayed by STO within our simulations under epitaxial strain constraints, although that shall be discussed more extensively in Chapter 5.

It must be noted that, while the B cation remains mostly isolated within the oxygen octahedron, the coordination landscape of the A cation is greatly affected by these rotations, hence becoming an important factor regarding the stability of each system [75].

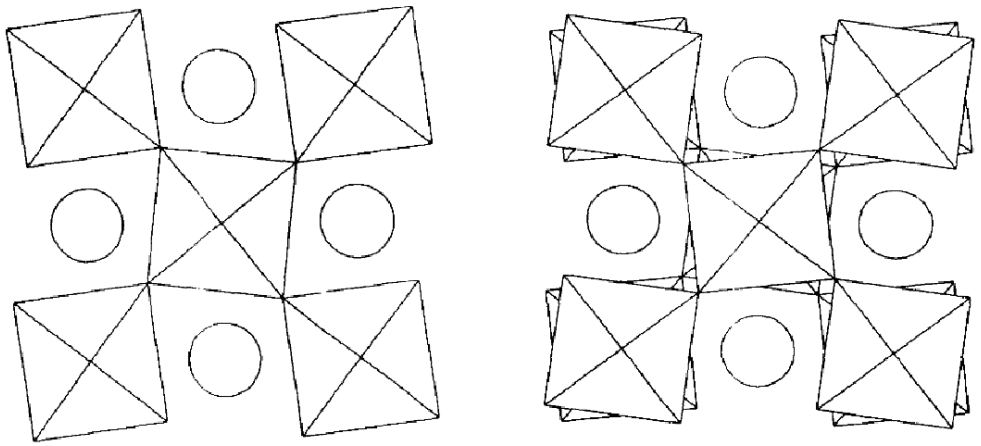

(a) AFD^i_z — $a^0a^0c^+$ **(b)** AFD^a_z — $a^0a^0c^-$

Figure 2.2: Depiction of the main AFD modes present in STO: the in-phase (a) and the anti-phase (b) rotation of the octahedra along the z axis. Images taken from Ref. [74].

II.ii Ferroelectric Mode

Within the 32 crystalline classes there are 21 with no inversion symmetry, out of which 20 exhibit piezoelectric behaviour (polarization fostered by mechanical stress). Among those there are 10 polar classes, showcasing a spontaneous permanent polarization P that varies with temperature, a property known as pyroelectricity. If the orientation of said polarization can be reversed under the application of a strong enough electric field, meaning there are two accessible equilibrium states, then ferroelectricity is achieved [36].

Regarding the nature of the ferroelectric phase transitions themselves one may also consider either the order-disorder type, where microscopic dipoles with originally random orientations suddenly align, or the displacive type, comprised by those where a small, collective displacement of individual atoms is required [36]. In this work we shall concern ourselves with the latter, given that displacements of the B cation within the oxygen octahedra are usually the origin of ferroelectric behaviour in perovskites, as shown in Fig. 2.3. The non-cubic surroundings of the O^{2-} ions seem to be the reason why perovskites are prone to this kind of transition, as suggested by local field calculations [36].

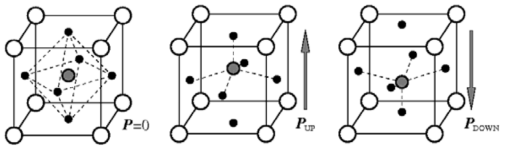

Figure 2.3: Depiction of a perovskitic ferroelectric mode, caused by the B cation's offset. Image taken from Ref. [**?**]

This ferroelectric mode generally arises only below a certain temperature associated to the phase transition, known as the Curie temperature T_0. We now proceed to explain the material's response in the vicinity of said transition.

Landau Theory of Ferroelectricity

A reliable description of the equilibrium behaviour of systems near a ferroelectric phase transition may be obtained using Landau theory, and it has indeed been used to obtain (phenomenologically) strain-temperature phase diagrams in ferroelectrics such as STO [56]. Although a much more in-depth description of this procedure can be found in [6] and many solid state physics textbooks [36], for the sake of completeness a few simple derivations and a brief summary of its main results are presented in this work:

As mentioned in Chapter 1, Landau theory is a symmetry-based analysis of physical systems in the vicinity of a phase transition. Landau stated in his 1937 papers [40] that a system cannot change smoothly between two phases of different symmetry. Additionally, the symmetry of one phase is required to higher than that of the other, due to thermodynamical arguments. The transition is subsequently characterized in terms of an order parameter, in this case the polarization P, that starts off at zero in the high-symmetry phase and becomes non-zero when symmetry drops.

The main simplifying assumption behind this theory is that the free energy $\mathcal{F}$ of the system near its phase transition can be expressed as a series expansion of the order parameter, although it is expected that this assumption breaks down at the transition point itself. Under these conditions, and assuming a uniform scalar polarization for the sake of simplicity, one may choose the following sixth order expansion as their initial ansatz

$$\mathcal{F}_P = \frac{a}{2}P^2 + \frac{b}{4}P^4 + \frac{c}{6}P^6 - EP, \tag{2.1}$$

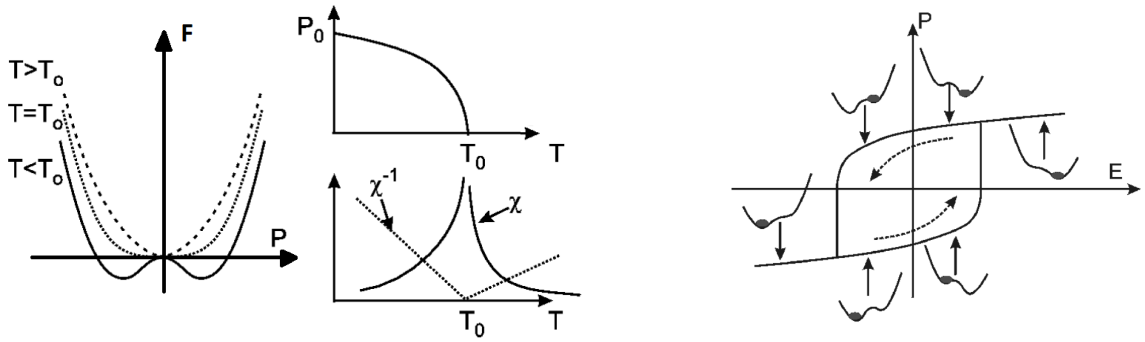

(a) Some relevant magnitudes. **(b)** Hysteresis cycle.

Figure 2.4: (a) Representation of the free energy $\mathcal{F}$, the polarization P and the dielectric susceptibility χ of a ferroelectric material near its critical temperature T_0. (b) Ferroelectric P-E hysteresis cycle along with several miniature representations of the system's free energy $\mathcal{F}$ at each step. Images taken from Ref. [6].

where only even powers are used due to symmetry considerations, as we assume the existence of two equivalent orientations in the polarization. Minimizing $\mathcal{F}$ in terms of P we obtain an expression for the electric field:

$$E = aP + bP^3 + cP^5. \tag{2.2}$$

Differentiating this equation with respect to P and setting $P = 0$ yields an expression for the dielectric susceptibility,

$$\chi = \frac{P}{E} = \frac{1}{a}. \tag{2.3}$$

In order to introduce the Curie-Weiss behaviour observed in ferroelectrics, we assume that around the Curie temperature $a = a_0(T - T_0)$, so that the expression for the dielectric stiffness κ matches experimental results:

$$\kappa = \frac{1}{\chi} = a_0(T - T_0). \tag{2.4}$$

If said assumption is introduced in Eq. (2.1) we obtain a temperature-dependant expression for the free energy,

$$\mathcal{F}_P = \frac{1}{2}a_0(T - T_0)P^2 + \frac{b}{4}P^4 + \frac{c}{6}P^6 - EP, \tag{2.5}$$

where a_0 and c are positive in all known ferroelectrics. Whether b turns out to be positive or negative determines the nature of the phase transition, either a second-order (continuous) transition or a first-order one, respectively. The temperature-dependent behaviour of the former is presented in Fig. 2.4a, where it can observed that below the Curie temperature two distinct polarization ground states emerge from a previously unpolarized one. The energy barrier between both polarizations means that small electric fields wont spontaneously change the polarization state of the system, meaning that even a simple model such as this one predicts ferroelectrical hysteresis cycles, as shown in Fig. 2.4b.

This description of ferroelectricity, known as Landau-Devonshire theory, is only appropriate for bulk systems with spatially uniform polarization, as it doesn't bode well with boundary conditions. Landau-Ginzburg theory solve those shortcomings by introducing power gradients in Eq. (2.1), extending its applicability to general bulk systems or thin film scenarios [6].

As a final note, were one to introduce strain coupling η in Eq. (2.1) as an additional order parameter several new effects would appear: second-order transitions may turn first-order ones, and the Curie temperature could vary considerably. Hydrostatic pressure may also reduce T_0, while biaxial stress may increase it (an effect observed in $BaTiO_3$ crystals) [6].

II.iii Driving Mechanisms

In this section we shall delve into some of the most generally accepted explanations for the appearance of these modes, starting from an empirical rule regarding ionic sizes and subsequently moving on to the influence of the chemical bonds and the lattice vibrational modes.

Goldschmidt Tolerance Factor

No discussion about perovskite instabilities may be complete without mentioning the Goldschmidt tolerance factor [21], an empirical rule quite ubiquitous throughout the existing literature. It is a dimensionless number that quantifies the stability of a given perovskite oxide, or alternatively the likelihood that it undergoes any structural distortion, based solely upon steric arguments regarding the ionic radii of its constituent atoms.

Under compact sphere packing conditions, the following relations may be extracted from simple geometric arguments emanating from the cubic perovskite BO_2 and AO planes, as depicted in Figure 2.5:

$$\begin{aligned} a &= 2r_B + 2r_O \\ a\sqrt{2} &= 2r_A + 2r_O \end{aligned} \tag{2.6}$$

where a is the cubic lattice parameter and r_i corresponds to the ionic radius of each atomic species. Substituting one in the other yields the definition of the (ideal) Goldschmidt tolerance factor:

$$t = 1 = \frac{1}{\sqrt{2}} \frac{r_A + r_O}{(r_B + r_O)} \tag{2.7}$$

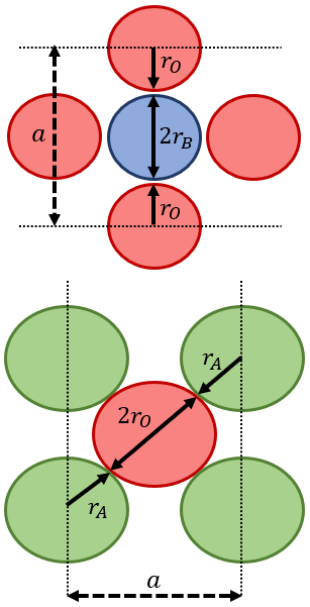

Figure 2.5: Visual derivation of the GTF.

Goldschmidt showed [21] that any perovskite composition where $t \neq 1$ -that is, differing from the proportions of an ideal cubic perovskite- will undergo structural distortions that improve the purportedly sub-optimal bonding conditions. While a tolerance factor t larger than unity indicates an relatively undersized B cation, rendering B-O polar distortions such as the ferroelectric mode more likely, $t < 1$ indicates a relatively undersized A cation, meaning enhanced A-O motion and consequently a much higher probability to display some sort of Glazer rotational system [7].

Making use of the ionic radii stated by Shannon in [65], we can observe that STO displays a tolerance factor barely larger than one ($t = 1.009$), which corresponds nicely with the fact that STO displays a cubic structure until it reaches its transition to the $a^0a^0c^-$ Glazer system.

As one would expect, it has been shown that there is a correlation between the magnitude of the tolerance factor and the energy difference between the aristotype and the ground state [7]. The amplitude of the octahedral rotations also exhibits a similar trend.

Chemical Bonding

Bonding properties between each the constituent atomic species within the perovskite are instrumental when it comes to understanding which of the 23 Glazer rotation systems it will display. As several explanations linking the nature of the bonds and the tilting of the oxygen octahedra have been proposed over the years, from a pseudo Janh-Teller effect [14] to a group-theoretical analysis of deviations from the aristotype cubic structure ($Pm\bar{3}m$) [29], a thorough discussion of them all vastly exceeds the scope of this work. Nonetheless, for the sake of completeness we shall attempt to summarize below the most remarkable conclusions offered by these studies.

Although both ionic and covalent bonding have been studied, the structures maximizing the latter will be the most stable overall. We may then split our discussion into the properties of A-O and B-O bonding.

Due to the sizeable difference in electronegativity between typical A atoms and O atoms, one would expect their bond to be highly ionic. A cations of increasing electronegativity will enhance the covalent nature of this bond, an effect magnified by deviations from the aristotype $a^0a^0a^0$ structure due to the increased overlap between the A and O orbitals. The orthorhombic $a^+b^-b^-$ system, already accounted for as the most common amongst the 23 Glazer systems, has been shown to maximize the covalent nature of this bond while minimizing its repulsive overlap. Hence this structure will be favored by perovskites sporting either a low enough Goldschmidt factor ($t < 0.975$) or a relative electronegative A cation, such as calcium [75].

On the other hand, since AFD rotations do not change the coordination sphere of B cations and the deformations in the oxygen octahedra are usually negligible, for the most part due to an increased bond strength stemming from a typically higher electronegativity compared to the A cation, they do not usually play an instrumental role in terms of determining the rotation system. Despite the fact that both B-O σ and B-O π covalent interactions (the later being only relevant when B is a transition metal) decrease with the B-O-B angle (180º in the cubic aristotype), their effects are relatively small for low tilt angles, and may be compensated by either ionic energy or covalency gains in the A-O bond [75]. This renders the ideal cubic structure unstable and therefore comparatively rare, as previously mentioned.

Soft-Mode Theory

Another approach towards understanding the structural instabilities of perovskite oxides was proposed in 1959 by Cochran et al. [8], based upon the idea that perovskites become unstable against a set of normal vibrational modes (the so called "soft modes") in the lattice. Basically, a given transition is characterized by one of these soft modes, whose frequency decays rapidly approaching T_0, reaching zero at the exact temperature. This means that the restoring force for that specific displacement pattern -related to some generalized elastic constant- softens, hence the naming choice [59]. This effectively establishes positive frequencies as a requirement for crystal stability [8], something which can be easily visualized through the computation of the phonon dispersion bands, such as those in Fig. 2.7.

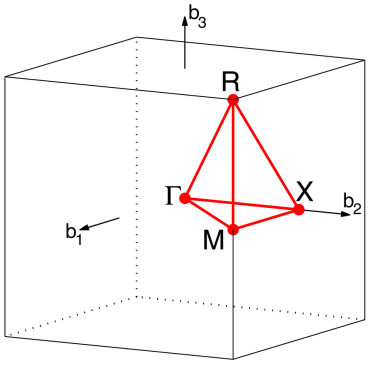

Figure 2.6: Brillouin zone of a Primite Cubic (CUB) unit cell. Image taken from Ref. [64].

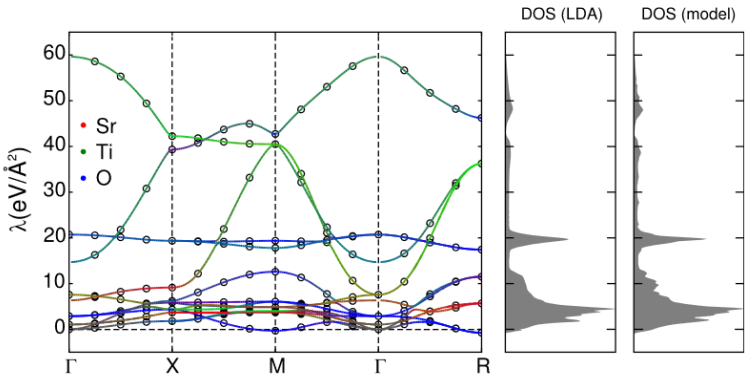

Figure 2.7: Phonon dispersion bands of cubic STO (left) calculated from first principles (lines) and from our second principles model (circles). On the left, the projected density-of-states (PDOS) obtained via both mechanisms. Image taken from Ref. [27].

Said figure contains the computed dispersion bands for our STO model, where we can see the R-point mode frequency drop below zero, corresponding to the AFD^a phase transition. The location of the soft mode in the Brillouin zone (hereinafter BZ, see Fig.2.6) has several implications regarding the nature of the phase transition. Whilst zone-center (Γ) soft modes, such as the FE mode, represent transitions in which the number of atoms per unit cell remains unchanged; zone-boundary (in this case R and M points, corresponding to the AFD^a and AFD^i instabilities respectively) soft-modes imply an integer multiplication (a doubling in the case of STO, see Fig. 4.2) on the number of atoms per unit cell below the critical temperature [59].

Further, the symmetry of the associated BZ point also affects the translational symmetry of the mode itself, something specially relevant when it comes to projecting the modes onto the system's equilibrium geometry: while the AFD^i mode (M-point) alternates sign for every unit cell displacement in the plane perpendicular to the rotation, the AFD^a mode (R-point) does so in every direction and the FE mode (Γ-point) doesn't do it at all (more in Chapter 4).

One of the most commonly accepted explanations for STO's incipient ferroelectricity, also known as quantum paraelectricity, comes from soft mode theory. Quantum fluctuations allegedly stabilize the soft mode, preventing it from reaching zero at the transition temperature as would happen in a paradigmatic ferroelectric (see Fig. 2.8). The relative permittivity subsequently plateaus instead of diverging, as expected in a conventional ferroelectric (see Fig. 2.4a), until reaching a temperature below which quantum effects complete cancel out the onset of ferroelectricity and the permittivity remains constant. In the case of STO this happens at around 4K [51].

Additionally, a link between this theory and the divergent behaviour of the dielectric susceptibility χ in ferroelectrics, predicted by Landau theory, may be found in the Lyddane-Sachs-Teller relation

$$\frac{\omega_{\mathrm{LO}}^2}{\omega_{\mathrm{TO}}^2} = \frac{\chi(T)}{\chi_\infty}, \tag{2.8}$$

where the ratio between the longitudinal and transverse optical frequencies of the soft mode is equal to that of the dielectric susceptibility $\chi(T)$ and its value in the visible range χ_∞. This and other arguments lead to this theory being considered a small but significant extension of Landau's theory of second order phase transitions [59].

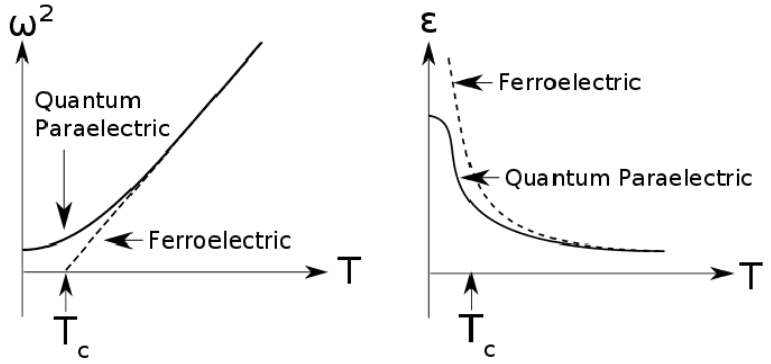

Figure 2.8: Comparison of the soft mode frequency ω and the dielectric constant ϵ between a quantum paraelectric (such as STO) and a typical ferroelectric material in the vicinity of the critical temperature T_c.

As a final note, one of the main setbacks in soft mode theory, as presented by Cochran [8], is that anharmonic interactions become highly relevant near the transition temperature T_0, meaning that one can no longer work within the framework of the harmonic oscillator.

II.iv Mode Competition

Although presented as isolated phenomena until now, there is extensive evidence of intrinsic couplings between the FE and AFD instabilities. Even though the former ends up suppressed in bulk STO by quantum effects (first-principles calculations predict a ferroelectric transition, which disappears when these effects are introduced via Monte Carlo path-integral simulations), it has also been shown that in the absence of AFD rotations STO does indeed display ferroelectric behavior [61]. Further, increasing crystal volume was seen to enhance FE distortions while weakening the AFD ones, suggesting a competitive relationship between both instabilities [61]. This competition though, present in many perovskites, turns into cooperation for large enough octahedral tilts in compounds with tolerance factors in the $0.78 < t < 1$ range [24]. This cooperation was found to be independent of strain, and based purely on steric arguments.

Quantum fluctuations in STO were found to have a much stronger effect on the FE transition than on its AFD counterpart, completely suppressing the former while barely affecting the transition temperature of the latter [77]. Other similar compounds such as $BaTiO_3$ are far less influenced by these quantum effects, ostensibly due to their substantially higher transition temperatures [77]. In fact, STO is so close to being ferroelectric that a simple isotopic exchange, oxygen-18 instead of oxygen-16, triggers a transition at around 25K [5], which is yet another reason why both modes are intertwined.

Finally, a discourse on the relationship of these instabilities would not be complete without mentioning improper ferroelectricity, a phenomenon whereby the layering of polar and non-polar perovskites (such as $PbTiO_3$ and STO) displays ferroelectric behaviour due to the AFD/FE coupling, instead of relying solely on the FE instability [4]. This grants control over the temperature dependence of the polar order parameter, which may be used to obtain a high, almost temperature independent dielectric constant, something really desirable from a technological perspective [4].

CHAPTER 3

COMPUTATIONAL TECHNIQUES

All properties of matter can be understood through the behavior of atoms, molecules and solids. Modern computational methods have proved to be powerful tools towards acquiring said knowledge, granting not only explanations to known phenomena but even predictive power in some cases.

Nonetheless, such kind of simulation procedures generally require vast swathes of computing power, even for modest systems no bigger than a few hundreds atoms. The technique used throughout this work, known as Second-Principles Density Functional Theory (SPDFT) [16], implements a novel approach that allows simulations containing up to thousands of atoms with relative ease.

In this chapter we shall start from the ground up, building up from the Schrödinger equation towards the main concepts behind SPDFT, while describing the various approximations involved.

I First-Principles Simulations

First-principles simulations -also known as *ab-initio* simulations- have seen increasing popularity in the last few decades, on par with the ever-growing computational power available with the purpose of predicting and explaining the different properties (optical, vibrational, electronic, magnetic) of a given compound from elementary information about its structure and composition [16].

First of all, some clarifications need to be made regarding the notation used throughout this chapter. Atomic position vectors will be represented by an uppercase $\vec{R}$ with greek alphabet subscripts, while electronic ones shall do so with a lowercase $\vec{r}$ and latin subscripts. Furthermore, Hartree atomic units will be used in order to simplify the notation. In this unit system the electron charge e and its mass m_e, the reduced Plank constant $\hbar$ and the inverse Coulomb constant $4\pi\epsilon_0$ are all equal to one.

Properties of materials may be understood by looking at their atomic and electronic structure. Given that material systems are usually within the limits of non-relativistic physics [1], we shall approach their study by means of the Schrödinger equation:

$$\hat{\mathcal{H}}\Psi_A(\vec{R},\vec{r}) = E_A\Psi_A(\vec{R},\vec{r}) \tag{3.1}$$

By solving Eq.3.1 the eigenfunctions Ψ_A of the systems are obtained, allowing *in principle* the calculation of any physical property of the system. The Hamiltonian $\hat{\mathcal{H}}$ on Eq. 3.1 may be decomposed in several terms:

$$H = T_e + T_n + V_{ee} + V_{nn} + V_{en} + V_{ext} \tag{3.2}$$

corresponding to the kinetic energy of electrons T_e and nuclei T_n, the electrostatic potential between electrons V_{ee}, nuclei V_{nn} and electrons and nuclei V_{ne} and a possible external potential V_{ext}. Given a system formed by N electrons and M nuclei, their expressions are denoted by the following equations:

$$\begin{aligned} T_e &= -\sum_i^N \frac{1}{2}\vec{\nabla}^2\vec{r}_i & T_n &= -\sum_i^M \frac{1}{2M_i}\vec{\nabla}^2\vec{R}_i \\ & & V_{ne} &= \frac{1}{2}\sum_{i,\alpha}^{N,M} \frac{Z_\alpha}{|\vec{R}_\alpha - \vec{r}_i|} \\ V_{ee} &= \frac{1}{2}\sum_{i,j}^N \frac{1}{|\vec{r}_i - \vec{r}_j|} & V_{nn} &= \frac{1}{2}\sum_{\alpha,\beta}^M \frac{Z_\alpha Z_\beta}{|\vec{R}_\alpha - \vec{R}_\beta|} \end{aligned} \tag{3.3}$$

In addition to the complexity of solving this equations even for a few atoms, due to the presence of cross terms in the expressions of V_{ee}, V_{nn} and V_{ne} no analytical solution can be obtained. Therefore, approximations need to be made in order to obtain sensible results.

I.i Born-Oppenheimer Approximation

This approximation relies on the fact that nuclei are far more massive than electrons, from which stems the assumption that they will also move far more slowly. This means that, at first approach, the movements of electrons and nuclei may be uncoupled and considered independent from each other [32]. The wave function $\psi_A(\vec{R},\vec{r})$ can then be decomposed as a product of electronic $\psi_e(\vec{r})$ and nuclear $\psi_n(\vec{R})$ wave functions: $\psi_A(\vec{R},\vec{r}) = \psi_n(\vec{R})\psi_e(\vec{r})$.

This allows the redefinition of the Hamiltonian (Eq.3.2) as the sum of the nuclei's kinetic energy and an electronic Hamiltonian:

$$\hat{\mathcal{H}} = T_n + \hat{\mathcal{H}}_e \qquad \hat{\mathcal{H}}_e = T_e + V_{ee} + V_{nn} + V_{en} \tag{3.4}$$

and the decomposition of the stationary Schrodinger equation into two separate equations

$$\hat{\mathcal{H}}\Psi(\vec{R},\vec{r}) = E\Psi(\vec{R},\vec{r}) \Rightarrow [T_n + \hat{\mathcal{H}}_e]\psi_n(\vec{R})\psi_e(\vec{r}) = E\psi_n(\vec{R})\psi_e(\vec{r}) \tag{3.5}$$

The first one corresponds with the eigenvalue equation for the electronic Hamiltonian $\hat{\mathcal{H}}_e$, a differential equation taking electronic positions as variables and atomic positions as parameters only:

$$\hat{\mathcal{H}}_e\psi_e(\vec{r}) = E_A(\vec{R})\psi_e(\vec{r}) \tag{3.6}$$

Both the eigenstates $\psi_e(\vec{r})$ and the eigenvalues $E_A(\vec{R})$ obtained depend parametrically on the positions of the atoms. Rewriting Eq.3.5 we obtain:

$$[T_n + E(\vec{R})]\psi_n(\vec{R})\psi_e(\vec{r}) = E\psi_n(\vec{R})\psi_e(\vec{r}) \tag{3.7}$$

In order to uncouple both equations, the effect of the momentum operator of the nuclei on the electronic wave functions must be neglected:

$$T_n\psi_e(\vec{r}) \approx 0 \tag{3.8}$$

This is the core statement of the approximation, justified by the fact that even in the case of the lightest possible nucleus, atomic hydrogen, the nuclear mass is around 1836 times that of the electron. This alone makes it possible to disregard atomic motion when considering the electrons only.

Under this considerations Eq.3.7 may be rewritten so as to obtain the following eigenvalue equation for the nuclei:

$$[T_n + E_A(\vec{R})]\psi_n(\vec{R}) = E\psi_n(\vec{R}) \tag{3.9}$$

where $E_A(\vec{R})$, the eigenvalues from Eq. 3.6, represent the potential affecting the nuclei due to their interaction with the electronic cloud surrounding them. Hence each arrangement of the nuclei $\vec{R}$ has its own potential field, known as *Adiabatic Potential Energy Surface* or APES for short. These surfaces are independent under the aforementioned conditions for the adiabatic approximation. Were two electronic states $\psi_e(\vec{r})$ to have similar enough APES then whole approximation would break down, as the correlation between them wouldn't be negligible [32].

All in all the Born-Oppenheimer approximation is an instrumental tool in first-principles simulations, as it simplifies the calculation of the stationary states of the system. It requires only the solution of two uncoupled differential equations, turning the original problem into a two-step process: First off the electronic equation (Eq.3.6) is solved, granting the APES $E(\vec{R})$ needed for the resolution of the nuclear equation (Eq.3.9). Were it not to be used (namely, were it not applicable to the system at hand), a complex system of coupled nuclear and electronic equations would need to be solved.

II Hartree-Fock Method

The problem now lies in finding the solutions ψ_e to the electric equation (3.6). This is a highly non-trivial task, as its a 3N-dimensional equation with no general analytic solution (besides one-electron systems) due to the presence of cross-terms in the electronic repulsion term $V_e e$.

This means its resolution requires the use of variational methods, particularly the Rayleigh-Ritz method [41]. They are based [32] on the fact that the energy E_t obtained with a trial wave function ψ_t will always be greater than or equal to energy obtained with the exact solution E_{ex}:

$$E_t = \langle\psi_t|\,\hat{\mathcal{H}}_e\,|\psi_t\rangle \geq E_{ex} \tag{3.10}$$

This trial wave function is a combination of N independent wave functions, each associated to a given electron and therefore independent of the positions of the others (for example, composed of hydrogen-like orbitals). This trial wave function is then variationally optimized until a minimum energy is found.

In 1928 Hartree [26] introduced a procedure, which he named self consistent field method (SCF), where the electronic wave function was approximated by a product of atomic orbitals:

$$\Psi(\vec{r}_1, \vec{r}_2, ..., \vec{r}_N) = \psi_1(\vec{r}_1)\psi_2(\vec{r}_2)...\psi_N(\vec{r}_N) \tag{3.11}$$

Although this greatly simplifies calculations, it does not comply with Pauli's exclusion principle because the wave function is not antisymmetrized under the permutation of two electronic positions, as Slater pointed out in 1930 [66]. This is solved through the implementation of the Slater determinant (Eq. 3.12), at which point Hartree's approximation becomes the Hartree-Fock (HF) approximation:

$$\Psi(\vec{r}_1, \vec{r}_2, ..., \vec{r}_N) = \frac{1}{\sqrt{N!}} \begin{vmatrix} \phi_1(\vec{r}_1) & \phi_2(\vec{r}_1) & ... & \phi_N(\vec{r}_1) \\ \phi_1(\vec{r}_2) & \phi_2(\vec{r}_2) & ... & \phi_N(\vec{r}_1) \\ ... & ... & ... & ... \\ \phi_1(\vec{r}_N) & \phi_2(\vec{r}_N) & ... & \phi_N(\vec{r}_N) \end{vmatrix} \tag{3.12}$$

Slater determinants are formed spin-dependent orthogonal orbitals, each independent from the rest, the notation $\phi_a(\vec{r}_b)$ representing electron a in position b. This formulation ensures Pauli's exclusion principle, as were two electrons to be in the same quantum state the determinant would equal zero. Hartree's approximation (Eq. 3.11) would correspond to the product of the diagonal elements of the Slater determinant. The configuration energy of the system may be obtained [32] by applying the electronic Hamiltonian $\hat{\mathcal{H}}_e$ to the Hartree-Fock wave function (3.12):

$$E = \sum_i h_i + \frac{1}{2} \sum_{ij} (J_{ij} - K_i j) + V_n n \tag{3.13}$$

where the one electron energy $h_i = \langle \phi_i | \hat{h}_i | \phi_i \rangle$, which includes both the T_e and V_{ne} terms, is given by:

$$\hat{h}_i = -\frac{1}{2} \sum_i \vec{\nabla}^2 \vec{r}_i - \sum_\alpha \frac{Z_\alpha}{\vec{R}_\alpha - \vec{r}_\alpha} \tag{3.14}$$

the other two terms, J_{ij} and K_{ij} correspond to the Coulomb potential and the exchange energy between electrons respectively:

$$J_{ij} = \int \int |\phi_i|^2 |\phi_j|^2 \frac{1}{|\vec{r}_i - \vec{r}_j|} d^3 r_i d^3 r_j \qquad K_{ij} = \int \int \phi_i^* \phi_j \phi_j^* \phi_i \frac{1}{|\vec{r}_i - \vec{r}_j|} d^3 r_i d^3 r_j \tag{3.15}$$

While J_{ij} corresponds to the classical electrostatic potential between electrons, K_{ij} is a purely quantum effect caused by the antisymmetrization of the wave function. It may be understood as a *Fermi hole* surrounding the electron, a region with low probability of finding another electron close by. It shall be noted that $J_{ij} >> K_{ij}$ for $i \neq j$ while $J_{ii} = K_{ii}$, hence no self-interaction terms arise.

Applying the variational principle (3.10) we can obtain a system of equations by minimizing the configuration energy with respect to the set of orbitals chosen for the Slater determinant:

$$\frac{\delta E}{\delta \phi_i} = 0 \quad \forall \phi_i \tag{3.16}$$

Solving said system yields [32] the Hartree-Fock equations:

$$\hat{F}_i \phi_i = \epsilon_i \phi_i \qquad \hat{F}_i = \hat{h}_i + \sum_i (J_i j - K i j) \tag{3.17}$$

where $\hat{F}_i$ are the Fock operators and ϵ_i the one-electron energies for each orbital considered. The process of optimizing the orbitals is an iterative self-consistent algorithm, known as SCF (for Self-Consistent Field), which goes as follows:

1. Initial estimation of the orbitals ϕ_i is made.
2. Find the solutions to the Hartree-Fock equations.
3. If the solutions differ from the estimations, go back to step 2 using said solutions as input.

The cycle finishes when the orbital variation goes below a certain threshold. It is important to note that different starting conditions for the orbitals may lead to different local minima in the energy. When the process is finished, the one electron-energies correspond to the eigenvalues in (3.17), and the total energy is just their sum [32].

The Hartree-Fock equations involve complex partial derivatives, hence numerical functions were initially used to solve them. In 1951 Roothan [60] first introduced an analytical expression for the orbitals. In molecules and solids this is known as LCAO (for Linear Combination of Atomic Orbitals), where each orbital ϕ_i is approximated as a linear combination of atomic orbitals χ_k:

$$\phi_i(\vec{r}) = \sum_k c_k \chi_k(\vec{r}) \tag{3.18}$$

Some relevant variations on this approximation are Slater-type orbitals (STOs) and Gaussian-type orbitals (GTOs), which expand the orbitals ϕ_i in terms of exponential and Gaussian functions respectively.

Furthermore special consideration is usually given to core orbitals, as they are usually not too relevant when it comes to chemical bonding. Generally they are either considered "frozen", with their c_k coefficients remaining constant, or they are outright substituted by an effective external potential applied on the valence electrons.

II.i Beyond Hartree-Fock

The HF approximation is not without its shortcomings. Electron–electron repulsion is only accounted for in an average fashion, and so the HF method is therefore also referred to as a mean-field approximation. This is due to the choice of using a single Slater determinant as the trial wave function [32]. Likewise it completely neglects electronic correlation, yielding a different energy for the system and rendering proper chemical bonding descriptions unfeasible:

$$E_{corr} = E_{real} - E_{HF} \tag{3.19}$$

One way of dealing with these issues is considering the HF approximation Ψ_{HF} as the first term on a series expansion of the system's wave function Ψ:

$$\Psi = c_0\Psi_{HF} + c1\Psi_1 + c_2\Psi_2 + ... \qquad |c_0|^2 >> |c_i|^2 \tag{3.20}$$

where Ψ_i are Slater determinants compatible with the system's geometry representing its excited states. There are other methods available, such as Møller-Plesset perturbation theory or coupled cluster methods, but they all lie beyond the scope of this work.

All HF-derived methods share the same downfall: performance. They all present prohibitively high computational complexity, as they need to deal with at least N three-dimensional wave functions (four-dimensional if electron spin is brought into the equation), while requiring even more than that in order to account for electron correlation. This means they are only suited for small molecules, rendering crystalline solid simulation unfeasible.

III Density Functional Theory

Due to the high computational demands of HF-based methods, a new approach was needed in order to tackle the simulation of medium-to-large molecules and solids. Density Functional Theory (DFT) was born during the mid-sixties, based on the idea that the system's energy can be expressed as a functional (that is, a function of a function) of electronic density $\rho(\vec{r})$.

This is a comparatively more intuitive approach, as electronic density is much simpler than the system's wave function ψ_e while containing all its information. It is a real observable that can be measured experimentally and contrasted with theoretical models. Furthermore, it also represents a significant reduction in the number of parameters: A wave function for an N electron system contains $4N$ variables, three spatial and one spin coordinate for each electron, whereas the electron density is the square of the wave function integrated over $N-1$ electron coordinates, each spin density only depending on three spatial coordinates *independently* of the number of electrons [9].

$$\rho(\vec{r}) = N \int |\psi_e|^2 d^3\vec{r}_2 ... d^3\vec{r}_N \tag{3.21}$$

The total energy of the system (3.4) is given [32] by:

$$E = \langle \hat{\mathcal{H}}_e \rangle = \langle T_e \rangle + \langle V_{ee} \rangle + \langle V_{en} \rangle + V_{nn} \Rightarrow \langle T \rangle + J + \langle V_x \rangle + E_c + \langle V_{en} \rangle + V_{nn} \tag{3.22}$$

where J is the Coulomb energy between electrons, $\langle V_X \rangle$ the exchange energy and E_c the electronic correlation. The terms $\langle V_{en} \rangle$ and V_{nn} are now considered as part of an "external" potential $V_{ext}(\vec{r})$ affecting the electron cloud, which can also include terms related to external magnetic or electric fields.

III.i Hohenberg-Kohn Theorems

In 1964 Hohenberg and Kohn [28] provided a solid mathematical foundation for DFT, hitherto an overlooked technique due to its lack thereof. While the first theorem states that the electronic density is indeed an equivalent variable to the wave function for the ground state, the second establishes a variational principle to obtain the ground state electronic density:

Theorem 1 (1st Hohenberg-Kohn (Existence) Theorem) *For the ground state there is a one-to-one correspondence between the electron density ρ and the nuclear potential $V_{ext}(\vec{r})$ (within a trivial additive constant), and thereby also with the Hamiltonian operator and the energy [32]. In other words, the energy is a unique functional of the electron density:*

$$E_0 = E_0[\rho]$$

It must be noted that, although in its original formulation the first theorem only contemplated non-degenerate ground states, its validity has also been proven for degenerate ground states and the least energetic excited states of any irreducible representation.

Theorem 2 (2nd Hohenberg-Kohn (Variational) Theorem) *The functional that delivers the ground state energy of the system gives the lowest energy if and only if the input density $\rho'(\vec{r})$ is the true ground state density $\rho(\vec{r})$. Hence a variational principle akin to (3.10) may be used to find the ground state electron density:*

$$E_0[\rho'(\vec{r})] \geq E_0[\rho(\vec{r})]$$

Despite the fact that these two theorems provided a much needed basis, at the time DFT was still lacking a reliable method to correctly calculate the total energy. This is where the contributions from Khon and Sham come in.

III.ii Khon-Sham Theory

The main setback of orbital-free DFT (as it has been hitherto presented) is the low quality of the kinetic $\langle T \rangle$ and exchange $\langle V_x \rangle$ energy functionals, usually obtained by considering a non-uniform electron gas such as in the Thomas-Fermi-Dirac (TFD) model. This in itself was another major flaw, as from a chemical perspective none of these theories predict any kind of bonding [32].

In 1965 Khon and Sham [37] suggested that the kinetic energy could be calculated using an auxiliary system S formed by N non-interacting electrons with the same electronic density and under the same effective potential $v_{eff}(\vec{r})$ as the system at hand. As we are considering independent electrons once again, we can utilize an independent orbital ψ_i^{KS} model as done previously in the Hartree-Fock approximation.

$$\left[-\frac{1}{2}\nabla^2 + v_{eff}(\vec{r})\right]\psi_i^{KS} = \epsilon_i^{KS}\psi_i^{KS} \tag{3.23}$$

The expression for the energy in the real system is therefore given by the following expression

$$E_{KS} = T_{KS} + J_{KS} + E_{XC} + \int n(\vec{r})v_{ef}(\vec{r})d^3\vec{r} \tag{3.24}$$

where the T_{KS} and J_{KS} terms correspond *exactly* to the kinetic and Coulomb energies of the electrons in the auxiliary system:

$$T_{KS} = \frac{1}{2}\sum_a \int (\psi_i^{KS})^* \nabla^2 \psi_i^{KS} d^3\vec{r} \qquad J_{KS} = \frac{1}{2}\int \frac{\rho(\vec{r})\rho(\vec{r}')}{|\vec{r}-\vec{r}'|} d^3\vec{r} d^3\vec{r}' \tag{3.25}$$

The term E_{XC} corresponds to the electron correlation and exchange energy, defined as the sum of the differences of the two previous terms between the real and auxiliary systems:

$$E_{XC} = (T - T_{KS}) + (E_{ee} - J_{KS}) \tag{3.26}$$

The difference in kinetic energy is implicitly assumed to be small, so that $(T - T_{KS}) \approx 0$. In the final integral, the term v_{ef} is given by the system's geometry (nuclei) and any external potential v_{ext} applied to the system, and it is formally defined [32] as:

$$v_{ef}(\vec{r}) = \frac{\delta J_{KS}}{\delta\rho(\vec{r})} + \frac{\delta E_{XC}}{\delta\rho(\vec{r})} + v_{ext} = \int \frac{\rho(\vec{r}')}{|\vec{r}-\vec{r}'|} d^3\vec{r}' + v_{XC} + v_{ext} \tag{3.27}$$

The only unknown term in equation 3.27 is v_{XC}, known as the exchange-correlation potential, is the main problem with modern DFT methods. As of yet there is no easy way to obtain such a functional, so approximations need to be made regarding its evaluation.

The most common approach -basically a reference point- is using an LDA (Local Density Approximation) potential, which considers an homogeneous electron gas of constant density for its derivation. In principle this only works for systems where $\rho(\vec{r})$ varies slowly, but it turns out to give good enough results for a wide variety of cases. This happens because it leads to a Fermi hole that, although imprecise, globally cancels self-interaction in the J term. This approximation splits E_{XC} into two contributions, one for exchange E_X and one for correlation E_C, which are calculated via Monte Carlo methods [54].

Next step in complexity would be a GGA (Generalized Gradient Approximation) potential, which takes into account not only local density of the gas ρ but also its gradient $\nabla\rho$ in order to tackle inhomogeneity. Other options include Meta-GGA, hybrid functionals that incorporate the exact exchange energy from HF methods, etc. The description of the aforementioned advanced methods is considered beyond the scope of this work.

IV Second-Principles Simulations

DFT-based first-principles methods have become the de-facto tool in modern times due to their high precision and predictive power. Nonetheless they also present important time and length scale limitations related to the computational complexity of the calculations involved (typically $\mathcal{O}(N^3)$), which make the simulation of systems larger than a few angstroms or for periods longer than a few femtoseconds pretty much unfeasible. In order to study this type of systems a new simulation procedure was developed, known as Second-Principles Density Functional Theory (SPDFT), allowing for calculations up to

IV.i Electronic Density

The main idea behind SPDFT is decomposing the electronic density $n(\vec{r})$ into two parts: a reference electronic density $n_0(\vec{r})$ (RED) which contains most of the electrons and a *deformation density* $\delta n_(\vec{r})$:

$$n(\vec{r}) = n_0(\vec{r}) + \delta n_(\vec{r}) \tag{3.28}$$

In non-magnetic systems $n(\vec{r})$ represents the ground state electronic density. In fact in most cases the ground state density is usually chosen as the system's RED, which is a parameter inside second-principles model and hence considerably reduces computing costs. This two-part formulation grants the ability to express the system's energy as a perturbative expansion as a function of electronic density:

$$E \approx E^{(0)} + E^{(1)} + E^{(2)} + ... \tag{3.29}$$

In order to determine the exact expressions of the $E^{(i)}$ terms we introduce the electronic density of (3.28) into (3.24), the DFT energy functional equation. As the terms representing electron kinetic energy and Hartree repulsion are linear with respect to electronic density the parts corresponding to the RED and the deformation density may be separated [16].

Unfortunately the term corresponding to the exchange and correlation energy is not linear with respect to electronic density, so an special treatment is required: in order to separate the reference and perturbative contributions we suppose the latter is really is small compared to the former, so that we can expand E_{XC} around the RED:

$$\begin{aligned} E_{XC}[n] = E_{XC}[n_0(\vec{r})] &+ \int \left.\frac{\delta E_{XC}}{\delta n(\vec{r})}\right|_{n_0} \delta n(\vec{r}) d^3\vec{r} \\ &+ \frac{1}{2}\int \left.\frac{\delta^2 E_{XC}}{\delta n(\vec{r})\delta n(\vec{r}')}\right|_{n_0} \delta n(\vec{r})\delta n(\vec{r}') d^3\vec{r} d^3\vec{r}' + ... \end{aligned} \tag{3.30}$$

IV.ii Energy Terms

Equation 3.29 is usually cut off at order two, each of the individual terms representing different physical contributions to the total energy. The base term $E^{(0)}$ is known as reference energy and corresponds exactly with the DFT energy of the system's ground state associated with the RED:

$$E^{(0)} = \sum_{j\vec{k}} o^{(0)}_{j\vec{k}} \left\langle \psi^{(0)}_{j\vec{k}} \right| \hat{T} + v_{ext} \left| \psi^{(0)}_{j\vec{k}} \right\rangle + \frac{1}{2}\int \frac{n_0(\vec{r} n_0(\vec{r}')}{|\vec{r} - \vec{r}'|} d^3\vec{r} d^3\vec{r}' + E_{XC}[n_0(\vec{r})] + E_{nn} \tag{3.31}$$

The first order term $E^{(1)}$ corresponds to the one-electron excitations originated from the electronic perturbation density $\delta n(\vec{r})$.

$$E^{(1)} = \sum_{j\vec{k}} \left[o_{j\vec{k}} \langle \psi_{j\vec{k}} | \hat{h}_0 | \psi_{j\vec{k}} \rangle - o^{(0)}_{j\vec{k}} \langle \psi^{(0)}_{j\vec{k}} | \hat{h}_0 | \psi^{(0)}_{j\vec{k}} \rangle \right] \tag{3.32}$$

Finally, the second order term $E^{(2)}$ corresponds to the two-electron contributions, namely the inter-electron interaction screened by the second order exchange and correlation term:

$$E^{(2)} = \frac{1}{2} \int \hat{g}(\vec{r},\vec{r}')\delta n(\vec{r})\delta n(\vec{r}') d^3\vec{r} d^3\vec{r}' \qquad \hat{g}(\vec{r},\vec{r}') = \frac{1}{|\vec{r}-\vec{r}'|} + \left. \frac{\delta^2 E_{XC}}{\delta n(\vec{r})\delta n(\vec{r}')} \right|_{n_0} \tag{3.33}$$

IV.iii Wannier Functions

The previous expressions for the energy were given in terms of Block orbitals, a highly delocalized base which stems directly from the Bloch theorem [1]. This makes them a natural choice for working with solids, as they share the periodicity of the crystal lattice. Computationally speaking though, this same delocalization makes them a suboptimal choice for simulation purposes. Wannier functions $|\chi_a\rangle$ present a much more convenient alternative for second-principles, and they are defined as follows [17]:

$$|\chi_a\rangle = \frac{V}{(2\pi)^3} \int_{BZ} d\vec{k} e^{-i\vec{k}\cdot\vec{R}_A} \sum_{m=1}^{J} T^{(\vec{k})}_{ma} |\psi^{(o)}_{m\vec{k}}\rangle \tag{3.34}$$

where V is the volume of the unit cell, $\vec{R}_A$ is the lattice vector of the cell where the Wannier function is located, J is the number of bands in the manifold and $T^{(\vec{k})}$ represents the unitary transformations affecting the Block orbitals $|\psi^{(o)}_{m\vec{k}}\rangle$. The following expression gives a series expansion of the Bloch wave functions in terms of the Wannier functions:

$$|\psi_{j\vec{k}}\rangle = \sum_a c_{ja\vec{k}} e^{i\vec{k}\cdot\vec{R}_A} |\chi_a\rangle \tag{3.35}$$

where the $c_{ja\vec{k}}$ coefficients are determined by imposing on $|\psi_{j\vec{k}}\rangle$ the condition of being Hamiltonian eigenstates.

Wannier functions may be obtained directly from first-principles [67], chosen so as to form an orthogonal basis for the calculations. Their high localization compared to Block functions (they are akin to their Fourier transform, after all) results in a reduced number of calculations, as only matrix elements between close neighbours need to be obtained. In fact, this basis choice alone considerably increases the computational efficiency of second-principles algorithms [16].

The electronic density may now be defined explicitly in terms of said Wannier basis as follows:

$$n(\vec{r}) = \sum_{ab} d_{ab} \chi_a(\vec{r}) \chi_b(\vec{r}) \tag{3.36}$$

where d_{ab} is the *occupation matrix*, related to the coefficients of the series expansion of the Block basis in terms of the Wannier basis (Eq. 3.35) and the occupation level $o_{j\vec{k}}$ of said orbitals:

$$d_{ab} = o_{j\vec{k}} c^*_{ja\vec{k}} c_{jb\vec{k}} e^{i\vec{k}(\vec{R}_A - \vec{R}_B)} \tag{3.37}$$

The *deformation matrix* D_{ab} is now introduced as a way to differentiate between the RED and the deformation density,

$$D_{ab} = d_{ab} - d_{ab}^{(0)}, \tag{3.38}$$

hence defining the latter as:

$$\delta n(\vec{r}) = \sum_{ab} D_{ab}\chi_a(\vec{r})\chi_b(\vec{r}). \tag{3.39}$$

Finally, we may rewrite the first and second order terms in the energy expansion as in terms of this new basis:

$$E^{(1)} = \sum_{ab} D_{ab}\gamma_{ab} \qquad \gamma_{ab} = \langle\chi_a|\,\hat{h}_0\,|\chi_b\rangle \tag{3.40}$$

The term γ_{ab} is equivalent to the hopping parameter in a typical tight binding model [1], quantifying the interaction between two electronic orbitals given by the Hamiltonian $\hat{h}_0$, associated the RED. The second order term also depends on the deformation matrix, as well as on the previously defined screening operator $\hat{g}$:

$$E^{(2)} = \sum_{ab}\sum_{a'b'} D_{ab}D_{a'b'}U_{aba'b'} \qquad U_{aba'b'} = \langle\chi_a\chi_{a'}|\,\hat{g}\,|\chi_b\chi_{b'}\rangle \tag{3.41}$$

It must be noted that all the expressions outlined in this section are only valid for non-magnetic systems, such as the one concerning this work. Magnetic systems require another term in the second order energy contribution, concerning spin polarization [16].

CHAPTER 4

METHODOLOGY

Whereas the last chapter gave a broad overview on the theory behind the simulations, this chapter aims to introduce the methodology followed in this work.

I Monte Carlo Simulations

The simulation of phase transitions requires the ability to carry out finite-temperature calculations, a task that is computationally prohibitive for most first-principles codes, which mainly focus on the optimization of the geometry of the system by some energy-minimization procedures.

One of the most common approaches when it comes to simulating finite-temperature systems is the use of what are known as Monte Carlo techniques. Owing their name to a famous casino in the city of Monaco, they are a class of computational algorithms that rely on the use of randomly generated numbers in order to perform their task. Although they were originally developed in the late 1940s in Los Alamos laboratory as a means to study neutron diffusion in fissile materials [49] (being of utmost importance in the development of the Manhattan project), they have seen widespread adoption in many areas of natural and social sciences. Some examples include the Metropolis-Hastings algorithm, used to sample statistical distributions whence direct sampling is complicated or unfeasible; simulated annealing algorithms, used to find global optima in functions with large search spaces, etc.

We harness these techniques to our advantage by means of a Markov chain procedure [39], obtaining at every step a new state for the system using the previous one as a starting point. A new position is randomly proposed for every atom in the supercell, consisting of a small, random displacement away from its previous position. The atomic movements are accepted based on the following Boltzmann probability

$$P(T) = e^{-\frac{\Delta E}{k_{\mathrm{B}} T}}, \tag{4.1}$$

where ΔE is the energy variation that the new position would imply, k_{B} is the Boltzmann constant, and T the absolute temperature under study. The energy variation is calculated with the second principles methods explained in Chapter 3, using the SCALE-UP implementation [16].

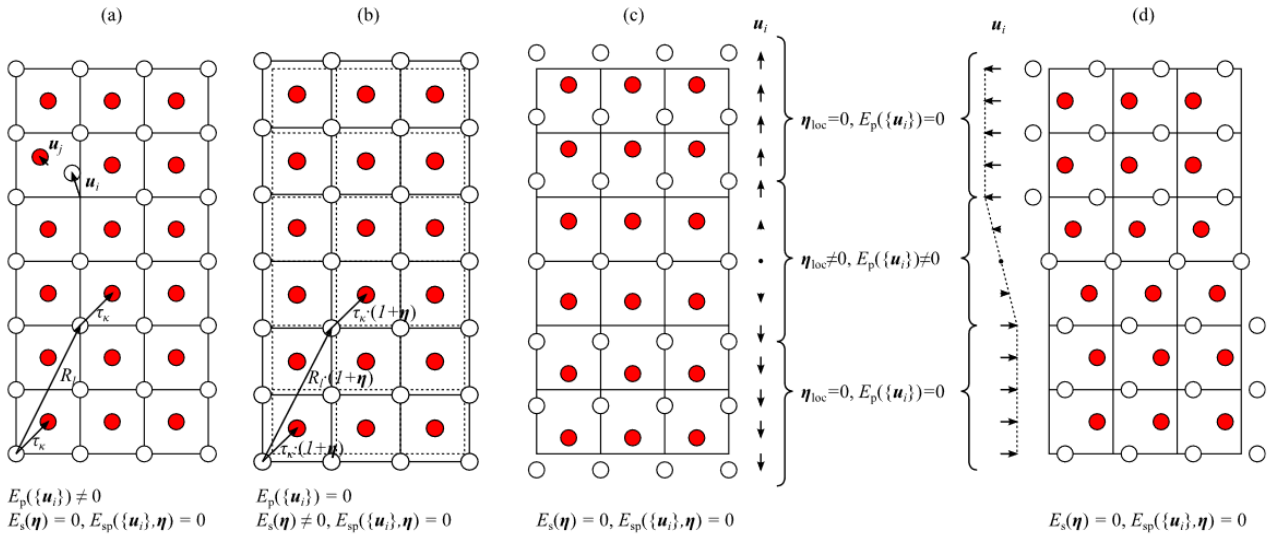

Figure 4.1: Schematic of the system's geometry under several types of distortions: individual atomic displacements (a), homogeneous strain (b) and inhomogeneous strain modelled as atomic displacements (c, d). Image taken from Ref. [27]

This means that if $\Delta E < 0$ the move is automatically accepted, but even if $\Delta E > 0$ (i.e. the movement implies an increase in the energy of the system), the new geometry can be accepted if $P(T) > r$, where r is a random number uniformly distributed between 0 and 1. Each iteration over all atoms counts as one single Monte Carlo step, a complete simulation being comprised of several thousands of them.

By the end of a given simulation, the displacements $\{\vec{u}_i\}$ of each individual atom (more precisely, those recorded after a number of *thermalization* steps) are averaged out, obtaining the *equilibrium geometry* (EG) of the system for that particular configuration[1]. Both the projection of the AFD and FE modes and the calculation of the system's polarization, procedures detailed in the following sections, are computed using this geometry.

It must be noted that the application of Monte Carlo methods to molecular modeling means that the dynamical behaviour of the system is overlooked in favor of its equilibrium state [39]. Although this does not interfere with our objective of finding the most stable phase in each configuration, it does indeed limit the range of application of this type of techniques.

I.i Geometry Definition

The geometry of the system within the second-principles framework is divided in two parts, similarly to how the electronic density $n(\vec{r})$ is also split into the RED $n_0(\vec{r})$ and the deformation density $\delta n(\vec{r})$. The position $\vec{r}_i$ of each atom in the supercell is given by

$$\vec{r}_i = (\mathbb{I} + \overleftrightarrow{\eta})(\vec{R}_i + \vec{\tau}_i) + \vec{u}_i = (\mathbb{I} + \overleftrightarrow{\eta})\vec{U}_i + \vec{u}_i, \tag{4.2}$$

where $\overleftrightarrow{\eta}$ is the strain tensor, $\vec{R}_i$ the position of the unit cell where atom i is located within the supercell, and $\vec{\tau}_i$ its position of atom i within the unit cell. These last two terms may be merged, obtaining its position within the *reference atomic geometry* (RAG) of the system $\vec{U}_i$.

[1]The term "configuration" meaning the simulation as defined by its set of experimental conditions, such as temperature or strain constraints.

The remaining term, $\vec{u}_i$, represents the displacement of each atom away from the reference structure after strain effects have been applied. The equilibrium displacement $\vec{v}_i$, equivalent to $\vec{u}_i$ in the EG, are obtained by averaging out $\vec{u}_i$ over N Monte Carlo steps,

$$\vec{v}_i = \frac{1}{N} \sum_{\text{step}=1}^{N} \vec{u}_{\text{step},i}. \tag{4.3}$$

In principle there are no restrictions concerning the choice of RAG. It is more convenient, however, to employ the ground state structure or some suitable high-symmetry configuration. Both of these choices correspond to extremes of the PES, meaning that internal forces and stresses on the cell are zero. Additionally, the higher the symmetry the fewer coupling terms (determined from first-principles simulations) are needed to describe the system [16]. In our case we used the aristotype structure as our RAG, with a cubic lattice parameter $a_0 = 3.845$ Å and the following atomic sites in each unit cell:

Species	Position
Sr	(0,0,0)
Ti	(1/2, 1/2, 1/2)
O_x	(0, 1/2, 1/2)
O_y	(1/2, 0, 1/2)
O_z	(1/2, 1/2, 0)

Table 4.1: STO atomic sites per unit cell.

Some additional comments shall be made regarding strain: The strain tensor $\overleftrightarrow{\eta}$, as presented above, is a triangular 6-element matrix, representing both shear and axial strain *homogeneous* components only. This strain is dimensionless, meaning each of the lattice parameters a_i may be simply obtained with $a_i = a_0(1 + \eta_i)$. Inhomogeneous strain is given by atomic displacement patterns, as shown in Fig. 4.1.

II Mode Projection

In order to measure the phase transitions present in STO we devised a generalized approach towards defining structural modes and projecting our equilibrium geometry onto them.

Starting from from the high-symmetry cubic perovskite structure, we define an structural mode as an specific pattern of atomic motions $\vec{P} = \{\vec{\nu}_i\}$ which may be comprised one or more unit cells Λ, centered on the Ti-atom. Each atomic motion $\vec{\nu}_i$ is normalized ($|\vec{\nu}_i| = 1$) and has a weight μ_i associated to it. Hence we define the amplitude a of the mode on a given unit cell Λ as

$$a_\Lambda = \sum_{i=1}^{M} \mu_i \left[\vec{\nu}_i \cdot \vec{v}_i(\Lambda)\right], \tag{4.4}$$

where the sum is taken over all the atoms M that take part in a particular mode. The specific values of the weights depend on the case at hand, and will be addressed shortly.

A graphical depiction of the modes under study in this work is shown in Fig. 4.2, while Table 4.2 contains a more thorough definition, weights included. In particular, the 'Hop' parameter

Atom	Hop	μ	$\vec{\nu}$
O_x	(0 0 0)	1/8	(0 1 0)
O_y	(0 0 0)	1/8	(-1 0 0)
O_x	(1 0 0)	1/8	(0 -1 0)
O_y	(0 1 0)	1/8	(1 0 0)
O_x	(0 0 1)	1/8	(0 1 0)
O_y	(0 0 1)	1/8	(-1 0 0)
O_x	(1 0 1)	1/8	(0 -1 0)
O_y	(0 1 1)	1/8	(1 0 0)

(a) AFD_z^i mode

Atom	Hop	μ	$\vec{\nu}$
Sr	(0 0 0)	1/8	(0 0 1)
Sr	(1 0 0)	1/8	(0 0 1)
Sr	(1 1 0)	1/8	(0 0 1)
Sr	(0 1 0)	1/8	(0 0 1)
Sr	(0 0 1)	1/8	(0 0 1)
Sr	(1 0 1)	1/8	(0 0 1)
Sr	(1 1 1)	1/8	(0 0 1)
Sr	(0 1 1)	1/8	(0 0 1)
Ti	(0 0 0)	1	(0 0 1)
O_x	(0 0 0)	1/2	(0 0 -1)
O_x	(1 0 0)	1/2	(0 0 -1)
O_y	(0 0 0)	1/2	(0 0 -1)
O_y	(0 1 0)	1/2	(0 0 -1)
O_z	(0 0 0)	1/2	(0 0 -1)
O_z	(0 0 1)	1/2	(0 0 -1)

(b) FE_z mode

Atom	Hop	μ	$\vec{\nu}$
O_x	(0 0 0)	1/8	(0 1 0)
O_y	(0 0 0)	1/8	(-1 0 0)
O_x	(1 0 0)	1/8	(0 -1 0)
O_y	(0 1 0)	1/8	(1 0 0)
O_x	(0 0 1)	1/8	(0 -1 0)
O_y	(0 0 1)	1/8	(1 0 0)
O_x	(1 0 1)	1/8	(0 1 0)
O_y	(0 1 1)	1/8	(-1 0 0)

(c) AFD_z^a mode

Table 4.2: Definition of the modes under study. While the first two columns denote the atomic species and the unit cell hopping, μ are the weights and $\vec{\nu}$ the normalized atomic motions.

contained in Table 4.2 represents a unit cell displacement, indicating where the corresponding atom in the pattern lies relative to the unit cell Λ where the projection is taking place.

While the FE mode is basically the movement of all Sr and Ti atoms in the opposite direction to that of the oxygen atoms conforming the octahedron, the AFD modes consist of the in-phase or anti-phase movement of the oxygen atoms within the plane perpendicular to the rotation axis.

It must be noted that, although all the modes as presented are oriented in the polar (z) direction, their reorientation in the (x) and (y) directions is a relatively trivial task

On the matter of the weights several lines of thought were followed. In the case of the AFD modes the quantity of interest is the average value of the atomic displacements in the rotation plane, so that we can obtain the rotation angle of the octahedra:

$$\theta = \arctan\left(\frac{a_\Lambda}{d(\mathrm{Ti},\ \mathrm{O})}\right), \tag{4.5}$$

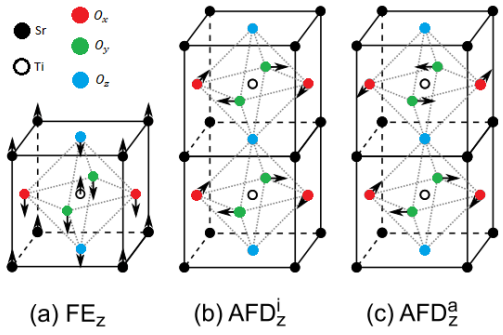

Figure 4.2: Sketch of the atomic displacements corresponding to the modes analyzed in this work: the ferroelectric (FE) distortion and both the in-phase (b) and anti-phase (c) antiferrodistortive (AFD) rotations. The z subscript denotes the polar orientation of the patterns. Image taken from Ref. [27].

where $d(\mathrm{Ti},\ \mathrm{O}) = |\vec{\tau}_\mathrm{O} - \vec{\tau}_\mathrm{Ti}|$ is the distance between titanium and oxygen atoms. Taking into account that we cannot consider the octahedra themselves as rigid due to the nature of Monte Carlo simulations themselves, the best estimate of the in-plane displacements is the average displacement of all the atoms composing the rotation. This is achieved by directly setting all weights to $\mu = 1/8$, as there 8 atomic motions $\vec{\nu}$ in each of the AFD modes.

On the other hand, in the case of the FE mode we are only concerned with the amplitude itself, rather than its use in a later calculation (the polarization derived from this mode requires other considerations, accounted for in the following section). Consequently the weights are targeted towards giving an accurate representation of this motion, dividing the contribution of each atom by the number of cells k wherein it participates in the calculation, that is $\mu = 1/k$.

As a practical example of this system, imagine we have a supercell with a perfect $a^0a^0c^+$ Glazer system, meaning there are only in-phase rotations along the z axis and no distortions in the oxygen octahedra. If one were to project the AFD_z^i mode on this supercell the contributions from the lower and upper octahedra would add up, returning the angle of rotation θ with Eq. 4.5. If we projected the AFD_z^a mode instead, the contributions from each octahedron would cancel each other out, meaning the rotation angle would be zero for that mode. Conversely, in a perfect $a^0a^0c^-$ Glazer system the two octahedra in the AFD_z^i mode would cancel each other out, while the angle obtained from the AFD_z^a would match the rotation angle as expected.

Finally, two relatively simple adjustments were made regarding AFD rotations for the sake of logical consistency. From a visual inspection of the patterns themselves as shown in Fig. 4.2 one can see that the projection of the AFD^a pattern on two adjacent cells with the same angle of rotation would yield equal amplitudes of opposite sign, resulting in opposite directions on the rotations. This is rather counter-intuitive, as the aforementioned hypothetical supercell displaying a perfect $a^0a^0c^-$ rotation system would yield amplitudes of alternating sign throughout the supercell. Similarly, projecting the AFD^i mode on adjacent cells in the $x-y$ plane presents a similar problem, as the perfect $a^0a^0c^+$ system would give columns of alternating sign.

Suitable prefactors were included in Eq. 4.4 [$p^a = (-1)^x(-1)^y(-1)^z$ and $p^i = (-1)^x(-1)^y$ for the AFD_z^a and AFD_z^i modes respectively, being (x, y, z) the position of Λ within the supercell] so as to counteract both these effects. It shall be noted that this situation stems directly from symmetry arguments regarding the location of the soft modes associated to these distortions in the Brillouin zone, as explained in Chapter 2.

III Polarization and Born effective charges

There are several approaches regarding the calculation of polarization, inspired by various models or descriptions of physical phenomena. Whilst the use of static charges, basically partitioning the electronic density between the different atoms, may seem like the most straightforward way, the fact that in most molecules and solids there is no set criterion as to where the boundaries between the ions lay makes them an ill-defined quantity. The concept of dynamic (or effective) charges is introduced as a means to solve this difficulty, defining them in terms of the polarization they produce (which can be measured experimentally) and not the other way around [18].

Within the realm of periodic solids, the Born effective charges are a tensor defined as a linear order proportionality coefficient between the macroscopic polarization in a given direction P_α and a cooperative atomic displacement $v_{i,\beta}$ in any given direction under the condition of zero macroscopic electric field,

$$Z^*_{i,\alpha\beta} = \Omega_0 \frac{\partial P_\alpha}{\partial v_{i,\beta}}\Big|_{E=0}, \tag{4.6}$$

where Ω_0 is the unit cell volume. The polarization may then be obtained by integrating along the atomic displacements. Assuming the effective charges $Z^*_{i,\alpha}$ remain mostly constant, this integral can be approximated by

$$P_\alpha = \frac{1}{\Omega_0} \sum_{i\beta} Z^*_{i,\alpha\beta} v_{i\beta}. \tag{4.7}$$

The Born effective charges used in this work are contained in Table 4.3 below. In our case the Born tensor is diagonal due to the symmetry of the system, hence only the main directions are shown. Further, due to the "acoustic sum rule" they all must add up (as vectors) to zero. This is easy to understand if one considers that a rigid displacement of all the atoms on a given direction should yield no polarization whatsoever [18].

As a side note, the polarization per unit cell in Chapter 5 was calculated using the same atomic pattern and weights as the ferroelectric mode in Table 4.2, purely for the sake of consistency in the domain plots (Figures 5.4 and 5.8) of the following chapter.

Species	Z^*_x	Z^*_y	Z^*_z
Sr	2.567	2.567	2.567
Ti	7.266	7.266	7.266
O_x	-5.707	-2.063	-2.063
O_y	-2.063	-5.707	-5.707
O_z	-2.063	-2.063	-2.063

Table 4.3: Born effective charges, in elementary charge e units.

CHAPTER 5

RESULTS

After having accounted for all the necessary explanations in Chapters 2 to 4, it is time to present the outcome of our own work, concerning the antiferrodistortive phase transition present bulk STO and its behaviour under epitaxial strain conditions.

I AFD Phase Transition under Strain-Free Conditions

As presented in Chapter 2, STO undergoes an antiferrodistortive phase transition from its high-temperature cubic structure to the $a^0a^0c^-$ Glazer system (tetragonal) when its temperature decreases below 105 K. With the intention of reproducing this phase transition in our simulations we monitored both AFD modes and the cell strains in the 20-400K temperature range, using $8 \times 8 \times 8$ supercells ($10 \times 10 \times 10$ in the simulations near the transition temperature, T_0) in Monte Carlo runs spanning 40,000 steps (80,000 respectively), 5,000 (10,000) of them being thermalization steps. This large supercells were intended to stabilize the system, as the rotation axis became unstable in smaller supercells due to the stochastic nature of Monte Carlo moves. This orientation flip became more likely near the transition temperature T_0, hence the increased simulation size in its immediate vicinity.

The results of the aforementioned simulation run are shown in Fig. 5.1, wherein the AFD^a rotations and the axial strains are presented as a function of temperature T. The AFD^i mode remained inactive throughout as expected, and was consequently omitted in this representation. The figure offers a clear view of the antiferrodistortive phase transition, albeit only qualitatively, as explained in the following paragraphs:

First of all the most, striking deviation from the experiments is the transition temperature T_0, sitting at around 330 K. Wojdel *et al.* [27] associate this outcome to a known overbinding issue related to the use of LDA functionals, a situation they attempt to rectify by introducing a negative hydrostatic pressure in their simulations. Despite these adjustments they failed to reproduce the 105K experimental value, obtaining a value for T_0 in the $\sim$160 K range. This discrepancy may be partly attributed to the fact that our approach treats the atoms as classical objects, negating any effects from zero-point quantum fluctuations. As shown by Zhong and Vanderbilt in [77] using model Hamiltonians from first-principles, quantum fluctuations may reduce T_0 by as much as 20 K.

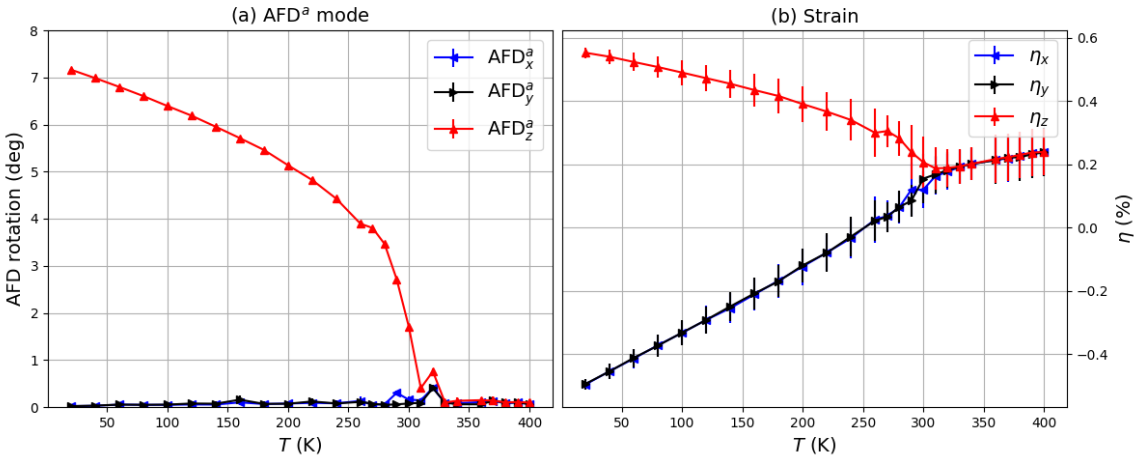

Figure 5.1: AFD^a rotation (a) and supercell strain η (b) in bulk STO with no strain restrictions.

Furthermore, while our model predicts a 7.2º rotation at low temperatures (20K), first-principles results [61] suggest a 5.5º rotation (0K) instead. Although the aforementioned overbinding correction brings it down to around 5.6º, in line with first-principles, they both still exaggerate the rotation when compared with experimental values [35] (2.0º at 1.5K).

This is a known problem with DFT methods, as they tend to overestimate this kind of octahedral rotations by as much as 20% depending on the functional of choice. LDA comes out as one of the worst in this regard, while hybrid functionals with relatively high HF exchange seems to significantly reduce this discrepancy [15]. STO in particular appears to be indeed highly sensitive to this choice, allegedly due to the anharmonic shape of its energy well and its relatively low transition temperature when compared to similar perovskites ($T_0 \geq 800$K).

Finally, in line with the previously mentioned overestimation of the tilting angles the tetragonality (c/a) is accordingly larger than the experimental value due to their intrinsic relationship. Our results display a low temperature tetragonality of $c/a \approx 1.007$, while it was experimentally determined [52] to be $c/a \approx 1.001$ instead. Further, a least-squares fit on the high-temperature ($T > 320$K) strains yields a linear expansion coefficient of $7.0 \cdot 10^{-6}$ K^{-1}, comparable to the value of $8.8 \cdot 10^{-6}$ K^{-1} obtained from experiments [52].

II Fixed-Strain Simulations

Other than the AFD transition present in unstrained bulk STO, we also studied its behaviour under expansive, static, and compressive epitaxial strain restrictions. Inside our simulations, this means the in-plane strain components η_x and η_y were locked during the simulation run to fixed values (+3%, 0% and −3% respectively) and their shared shear component η_{xy} was set to zero. Once more $8 \times 8 \times 8$ supercells were used, with simulations spanning 40,000 MC steps (5,000 for thermalization) in the 20-300 K temperature range.

As previously mentioned in Chapter 1, the behaviour of STO under epitaxial strain restrictions is highly relevant due to its widespread use as a substrate to grow other compounds, a situation where lattice mismatch effects are usually unavoidable.

In this section we shall analyze the AFD rotations and cell strain in all three cases, along with the polarization and FE displacements. Finally, a suitable phase diagram is provided as a means to condense all the relevant information.

II.i Expansive Strain

The application of expansive epitaxial strain in STO has reveled a complex landscape regarding structural transitions, phases and domains that we shall uncover shortly. However, before doing so several remarks need to be made about the figures in this section:

Due to the aforementioned domain structure displayed by numerous simulations, all the Figures present their respective quantity as the average of the absolute value on a per-domain basis. As an example, imagine there were to be two equally sized domains with a similar polarization but in opposite directions. While the net supercell polarization would vanish, our chosen criterion means that our Figures will display the absolute value of the polarization. This is also applicable to the representations within the static and compressive strain sections. Having settled this matter, we may begin with their corresponding analysis.

First of all, we may focus on the AFD rotations and cell strains presented in Fig. 5.2. The expansive strain conditions mean that the octahedra have much more breathing room for moving in the $x-y$ plane, hence only rotations within it are observed. The relationship between this in-plane rotations and the symmetry of the supercell is clear, as the strain's z component η_z remains negative throughout all temperatures as well.

The system starts off at low temperatures with equal AFD^a rotations in the x and y directions until it reaches a transition where one of them[1] dominates over the other, increasing in amplitude and cancelling the rotation in the other rotation. As we shall explained below, this phase with equal in-plane rotations also presents polarization in the (110) direction, which disappears when the transition takes place somewhere between 80 K and 110 K. From that point onwards the dominant rotation gradually decreases until the $a^0a^0a^0$ phase is reached at 300 K, although the previously cancelled rotation component briefly reemerges in the 210-240 K temperature range. The AFD^i rotation detected at low temperatures corresponds to domain walls within the supercell (Fig. 5.4), a pattern also seen under compressive strain restrictions (Fig. 5.8).

Moving onto the polarization and FE mode displacements (Fig 5.3), we can see that there is a clear correlation between he rotation of the oxygen octahedra around an axis contained in the plane and the existence of a polarization along the (110) direction, whose value, between 0.15 and 0.20 C/m^2, is qualitatively consistent with experimental results [25].

[1] As there is no way to control which direction the system chooses to stabilize, the largest $x-y$ plane rotation is always presented as being in the x direction for the purpose of visual clarity.

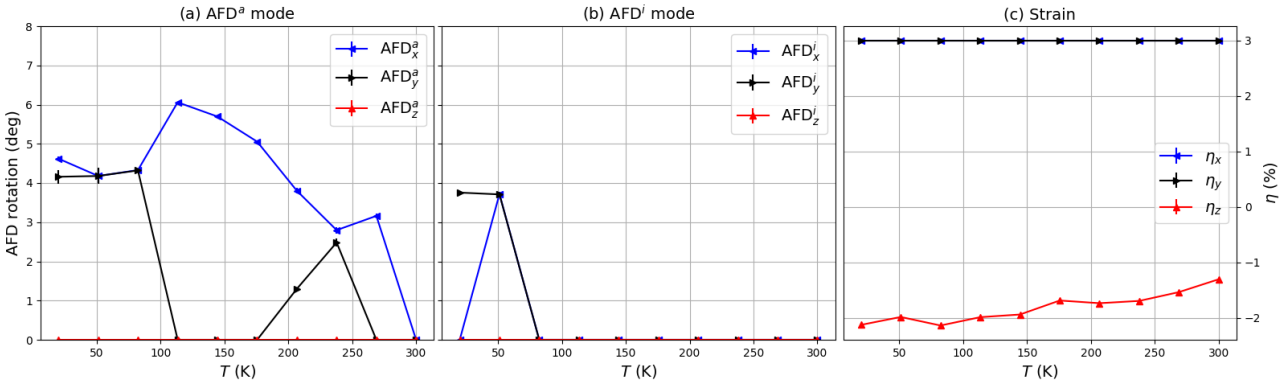

Figure 5.2: (a) Antiphase rotations (AFD^a), (b) in-phase rotations (AFD^i), and (c) homogeneous strain η in a supercell strain (η) in bulk STO under an expansive strain of 3%.

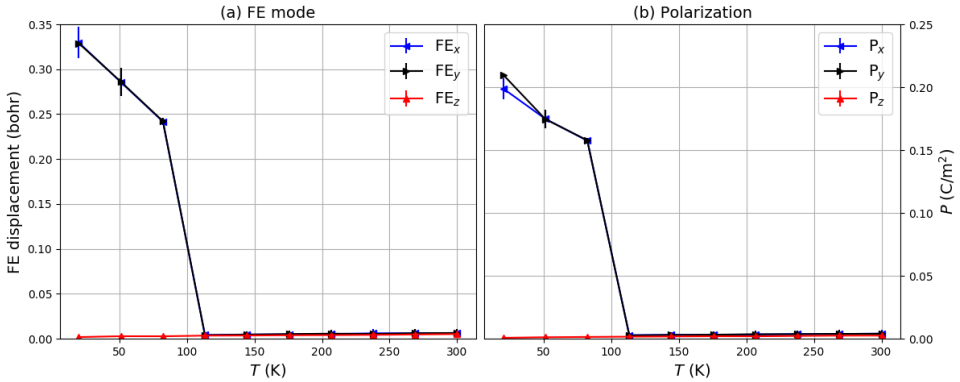

Figure 5.3: Ferroelectric displacements (a) and supercell polarization P (b) in bulk STO under expansive strain restrictions.

There is nonetheless a great deal to say about the domain structure present in the low-temperature polar phases, which can be observed in Figure 5.4. We may refer to the three simulations as T1 (20 K), T2 (50 K), and T3 (80 K), in order of increasing temperature.

At first sight we can observe that there is a clear correspondence between the axis of the AFD rotations and the direction of the polarization of the FE mode, at least in T1 and T3. T2 presents a more complex situation, that will be discussed in detail below. It is also straightforward to realize that the AFD^i rotations only appear in the domain walls between different AFD^a regions, a situation which will also show up under compressive strain constraints.

In T1 there are two distinct domains, each with AFD^a rotations and polarization perpendicular to each other. This kind of periodic structures[2], known as antiferrodistortive cycloids, have been related to the appearance of macroscopic polarization due flexoelectric[3] effects [62]. In these parallel domain walls, acting as ferroelectric twin boundaries, the order parameter -i.e. the rotation- changes direction by 90º (and hence vanishes at some point), leading to the activation of secondary ferroelectric instabilities which may otherwise be supressed by the AFD mode. This seems to be supported by the fact that the component of the polarization perpendicular to the domain wall (100) drops from 0.21 C/m^2 to 0.19 C/m^2 in the cells conforming the wall, leading to the slight discrepancy in Figure 5.3b which is not explained by the FE mode alone.

Moving onto T2, we can observe a complex domain structure characterized by point-like[4] charge accumulations associated to something resembling antiferrodistortive vortices. It must be noted, however, that these vortices correspond to the projection of the AFD^a mode as presented in Chapter 4, not just the rotation of the octahedra themselves. This becomes clear by looking at Fig. 5.5, where the rotation of individual octahedra (which may be considered a linear combination of both AFD modes) is presented against the aforementioned AFD^a mode projection.

Having made this distinction clear, and considering this domain configuration should be relatively unstable due to the charge defects, it is not far fetched to think of this phenomenon as somehow related to the recently predicted [22] and subsequently discovered [11] topological structures known as polar skyrmions.

[2]Considering the periodic boundary conditions of the supercell, this patterns does indeed repeat indefinitely.

[3]Flexoelectricity referring to the property whereby a material exhibits a spontaneous electrical polarization induced by some sort of strain gradient, in this case within the domain walls.

[4]More precisely column-like, as the pattern repeats vertically along the supercell.

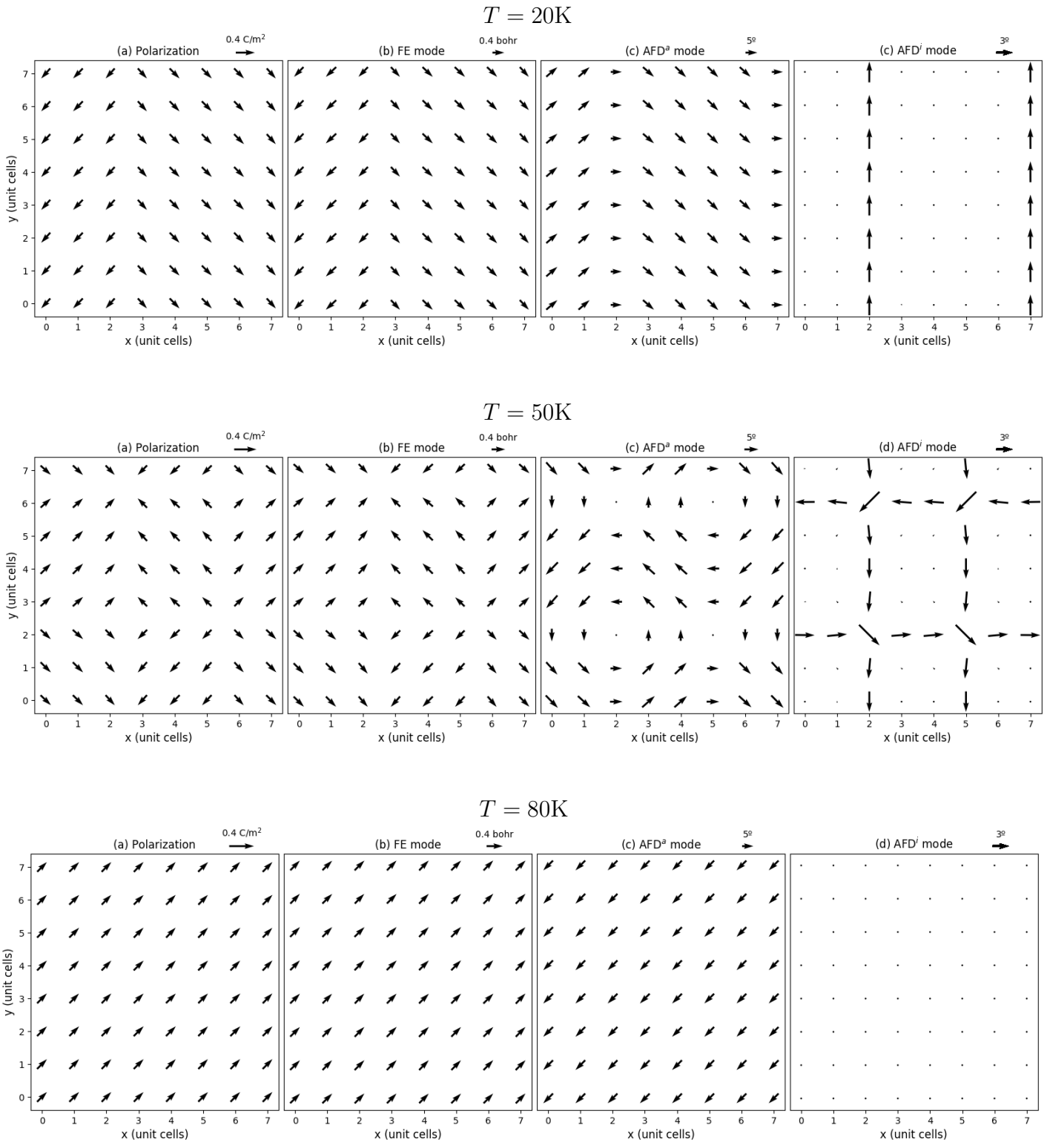

Figure 5.4: Domain representation of the polarization (a), ferroelectric displacements (b) and AFD rotations (c,d) per unit cell in the $x - y$ plane of bulk STO under expansive strain restrictions in the first three temperatures.

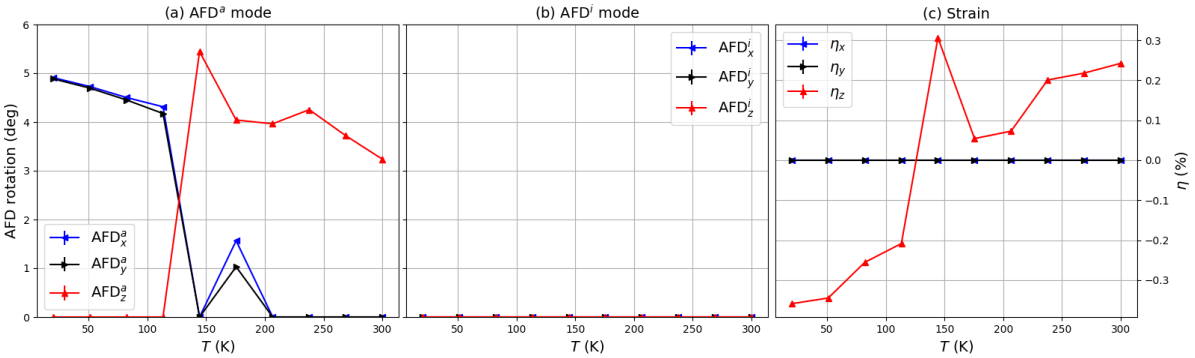

Figure 5.6: AFD rotations (a,b) and supercell strain η (c) in bulk STO under static strain restrictions.

They are the electric counterpart of magnetic skyrmions, a quasiparticle formed by a coordinated arrangement of spins (in our case, polarization domains) in the material. Their stability is usually attributed to some sort of 'topological protection', meaning they cannot rearrange themselves without overcoming a suitable energy barrier. Polar skyrmions are really interesting from a technological standpoint, due to their potential applications in the development of racetrack (domain-wall based) computer memory [22].

Finally, in T3 we can observe a paradigmatic monodomain structure, that we assume to be the true ground state of the system. The fact that T1 and T2 did not reach this situation stems directly from the random nature of Monte Carlo simulations, whose strong dependence of the first few random moves renders them unable to reach the lowest energy configurations consistently.

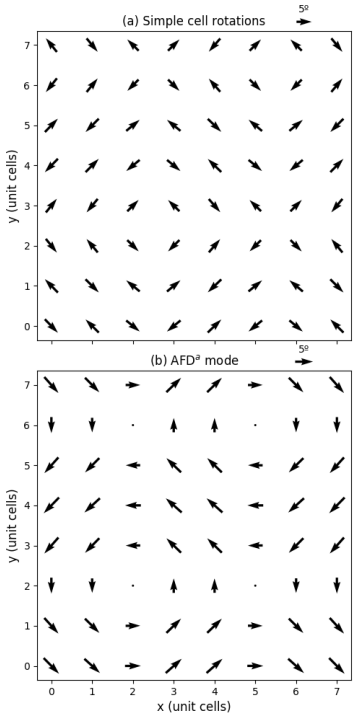

Figure 5.5: Simple octahedral rotations (a) beside their corresponding AFD^a mode rotations (b).

II.ii Static Strain

In this case no polarization is displayed by STO despite the fact that it boasts the same $a^-a^-c^0$ rotation system at low temperatures (Fig.5.6). There is nonetheless quite an interesting transition between 110 K and 140 K from rotations around an in-plane axis, AFD^a, to rotations around a vertical axis to vertical ones, accompanied by a shift in the tetragonality (η_z becomes positive). This doesn't but reinforce the position of the octahedral rotations as the main driving mechanism behind the unit cell's shape and symmetry, as explained in Chapter 2.

II.iii Compressive Strain

Last but not least, we observe a relatively 'monotonous' behaviour in STO under compressive strain, as only one phase is displayed. In Figure 5.7 we can see there are both AFD^a and AFD^i rotations in this setup, although no FE displacements nor polarization were detected. This is quite an striking situation, as it is generally assumed that STO displays and out-of-plane polarization when epitaxially compressed. While theoretical models based on Ginzburg-Landau theory [56] and experimental results [31] confirm this assumption within a thin-film scenario, as far as we are concerned only surface polarization -associated to relaxation effects- has been detected in bulk STO [3].

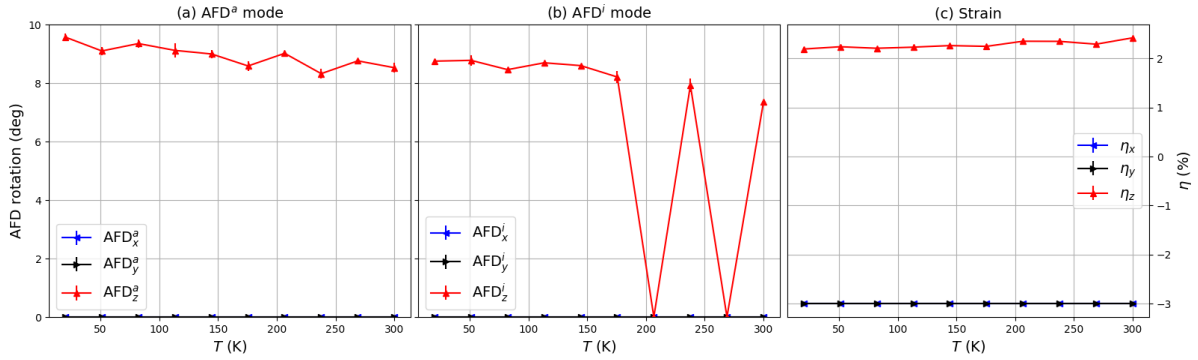

Figure 5.7: AFD rotations (a,b) and supercell strain η (c) in bulk STO under a compressive strain of -3%

.

The domain structure was similar throughout all temperatures, composed of horizontally stacked layers of AFD^a and AFD^i rotations along the z axis similar to those in Figure 5.8, except in two occasions ($T = 210$ K and $T = 270$ K) where a monodomain AFD^a system was observed. The z strain component η_z stays positive all the time, as one would expect from this rotation system.

Once more, these rotational layers are quite certainly not the state of minimum energy of the system, and are most likely just local minima in the PES. By inducing rotations in the starting geometry we observed that the system could indeed reach a monodomain structure at low temperatures (at 20 K). Nonetheless, the fact that these metastable configurations arise in pretty much every simulation we have carried out indicates that the energy barrier to escape these metastable local minima is rather high, so it is difficult to get out of the energy valley. This is corroborated by the fact that the only two cases were the monodomain configuration is the most accessed state occur at relatively high temperatures (210 and 270 K). Certainly, more statistics are required to clarify this issue, which unfortunately lies beyond the scope of the present work.

II.iv Phase Diagram

The information concerning all the phases observed in this section has been condensed into the phase diagram in Table 5.1, with all the appropriate information about the phases themselves contained in Table 5.2.

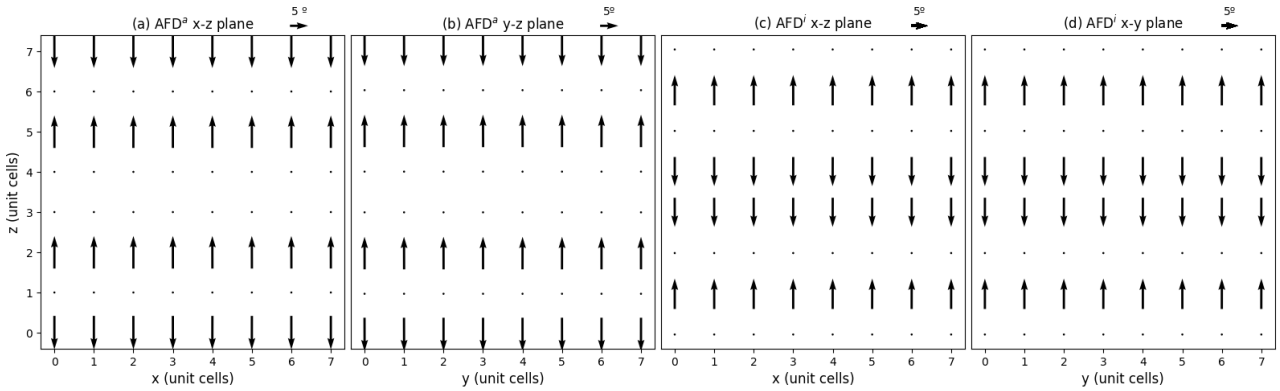

Figure 5.8: Representation of the AFD domain structure in the $x-z$ and $y-z$ plane of STO under compressive strain restrictions at a temperature of $T = 50$K.

η_{xy}											
+3%	IP2-FE+			IP1			IP2n		IP1	HT	
0%	IP2				OP						
-3%	OP+										
	20	50	80	110	140	170	210	240	270	300	T (K)

Table 5.1: Strain-temperature phase diagram of epitaxially strained STO.

In short, from our results we may classify the different phases in the sections above depending on whether they present in-plane (IP) or out-of-plane (OP) rotations, ferroelectric behaviour (FE) and/or domain structures (+). Additionally, in the case of in-plane rotations we may specify whether they present rotations in one direction (IP1), two equal rotations in both directions (IP2) or two unequal rotations each in one direction (IP2n). There is also a high-temperature tetragonal phase (HT), where neither AFD rotations nor ferroelectricity persist.

It shall be noted that the space groups included in Table 5.2, taken from the analysis carried out in Ref. [29], are simply those associated to each Glazer system without any additional considerations. Hence they may not be completely accurate, as it is generally assumed that the lattice parameters are determined by the rotation and not the other way around. As an example, consider the IP1 phase: an unrestrained $a^-b^0b^0$ system would generally have a lattice constant a along its rotation axis larger than that the other two, as opposed to the current situation where an external strain is imposed.

Comparing our phase diagram with the one presented by Pertsev *et al.* in [56], obtained by means of Ginzburg-Landau theory (introduced in Chapter 2), we observe some striking differences that are worth mentioning. We must note that their model does not contemplate the appearance of any domain structures, and although they only analyzed strains between -2% and 2%, these extreme cases should still be comparable to ours.

Firstly, under expansive strain both models coincide on the low-temperature scenario, with equal rotations and polarization in the $x-y$ plane. Similarities end there, as for higher temperatures

Phase	Glazer System	Space Group	Lattice	Domains
IP2-FE+	$a^-a^-c^0$	Imma	$a=b>c$	Yes
IP1	$a^-b^0b^0$	I4/mcm	$a=b>c$	No
IP2n	$a^-b^-c^0$	C2/m	$a=b>c$	No
HT	$a^0a^0c^0$	$Pm\bar{3}m$	$a=b>c$	No
IP2	$a^-a^-c^0$	Imma	$a=b>c$	No
OP	$a^0a^0c^-$	I4/mcm	$a=b<c$	No
OP+	$a^0a^0c^-$	I4/mcm	$a=b<c$	Yes

Table 5.2: Characteristics of the different stable phases contained in the diagram of Table 5.1.

they only predict another phase where the polarization remains but the rotations disappear, exactly the opposite to what we observe. Their approach does not predict our HT phase until far past 300K either, something unexpected considering our model's tendency to exaggerate transition temperatures (as seen under strain-free conditions).

Their model also predicts that our IP2-FE+ phase should remain stable under static strain restrictions, while within our model said phase loses its in-plane polarization (IP2 instead). In this same situation their model also predicts that an increase in temperature leads to a phase similar to IP1, although our predicted OP phase also lies really close in their diagram. This may be somehow related to the small $x - y$ plane rotations observed in Figure 5.6 at 170K, although additional statistics are needed in order to confirm this.

Finally, as mentioned in the previous section, Pertsev's calculations indicate there should be an out-of-plane polarization under compressive strain restrictions, in clear contradiction with our model. Although this may be related to the aforementioned layers of rotational domains, which are unaccounted for in their model, this may also be attributed to some other structural mode not contemplated in our calculations. Sadly, an appropriate resolution of this matter was outside the question mainly due to time-related limitations.

CHAPTER 6

FINAL CONSIDERATIONS

In this final chapter we shall summarize the main conclusions of this work, suggest additional improvements regarding our current methodology and introduce possible future lines of research.

I Conclusions

All in all, we managed to achieve all the objectives presented in Chapter 1: we successfully reproduced the antiferrodistortive phase transition qualitatively by means of second-principles techniques, in addition to obtaining a (sadly limited) temperature-strain phase diagram of STO.

Furthermore, in the process of obtaining said diagram we encountered several phases of STO with interesting domain structures, particularly when exposed to compressive and expansive strain restrictions. In the first situation we observed purely rotational domains in the out-of-plane direction, which might be related to the absence of ferroelectricity in bulk STO as opposed to the thin film scenario. On the latter case the domains observed under expansive strain involved an intertwine of both rotations and polarization, with charge defects associated to antiferrodistortive vortexes.

On the other hand, the lack of predictive power regarding transition temperatures proved to be underwhelming. Moreover, the fact that we observed domains in our simulations, although doubtlessly interesting, means that we cannot ensure the system reaches a global energetic minimum. Our systems become highly susceptible to the first few (random) deviations from it starting cubic structure, which ultimately determine the equilibrium structure due to the optimizing nature of Monte Carlo simulations, specially when considering low temperature scenarios. On the plus side this represents a significant control mechanism, as the appearance of a given metastable structure may be fostered through a simple modification of the system's starting geometry.

Finally, we demonstrated the capabilities of second-principles simulations when it comes handling large systems -between 2,500 and 5,000 atoms-, an unthinkable feat using traditional techniques. Due to the large amounts of data produced by these simulations, a Python package (more on Appendix A) was developed in order to manage and automate most of the analysis procedures.

II Improvements and Future Work

Although the results presented in this work are complete and self-standing, we had our share of complications derived from the COVID-19 pandemic when accessing our usual computational resources. This hindered our progress in this work, slowing down everything considerably.

Had the circumstances been different, a more thorough exploration of the strain-temperature grid would have yielded a interesting into how the different phases transform meld into each other, instead of just looking at the three "edge cases" of strain analyzed in this work. This would have also enabled the creation of a phase diagram much richer in detail than the one currently presented, and hence substantially more useful.

In addition to this, a comprehensive study on the energetics of the domain structures could have also been a worthy extension, seeing that appropriate modifications on the system's starting geometry could trigger its relaxation into either the minimum energy state or some sort of metastable domain configuration. This would require a complete statistical analysis of the states accessible to the system, something beyond the time limitations of this work. Furthermore, the effects of hydrostatic pressure and/or external electric fields on the domain formation process could have been considered, as this possibility was already accounted for within our code.

Finally, the antiferrodistortive rotational vortexes observed in Figure 5.4 definitely deserve a lot more attention and study than what could be spared for them during this work. In fact, due to their evident complexity and their potential from a technological standpoint, another whole new thesis could be written just about them.

APPENDIX A

CODE IMPLEMENTATION

As part of this work a Python package was developed in order to simplify the process of executing SCALE-UP simulations comprising a multi-dimensional parameter space, consisting of temperatures, strains, hydrostatic pressures and applied electric fields. The code itself is available both in GitHub (https://github.com/rcote98/ezSCUP) under GNUv3 license and within the CD containing this work. Installation can be performed on any operating system by just typing "`pip install ezSCUP`" within the command prompt, although downloading the full source code is recommended if its usage in another project is expected.

Essentially the goal of this package is to provide an easy way to schedule a large number of SCALE-UP Monte Carlo simulations, while organizing their output so as to enable access from Python itself. Even though the present work was (conceptually) relatively simple, as it involved solely simulations in a range of strains and temperatures, the sheer number of calculations involved would have been a nightmare to manage without this package.

I Structure

The main modules within the package, basically those a final user would come into contact with, are the following:

- **simulations.py:** Contains the main simulation class (MCSimulation), which carries out the simulations for a given parameter grid and creates a suitable folder structure to store all the output; and the main analysis class (MCSimulationParser), that grants access to the output of any given configuration in the parameter grid through Python itself.
- **analysis.py:** Contains all the code regarding mode projection, essential for analyzing AFD rotations and ferroelectric displacements. There is a general class for creating new projections as well as some specialized functions for the AFD and FE modes. There is also another class to calculate the polarization from Born charges, both supercell-wide and on a cell-by-cell basis.
- **settings.py:** General settings for the module as its behaviour. Simulations settings such as number of total and equilibration MC steps, the strain components to fix or how often partial files are printed out can by modifying the variables inside this file. A valid SCALE-UP executable need to be setup in order to run any simulations.

On the other hand, the following modules contain mainly auxiliary classes and functions, so they may not be as relevant for the final user.

- **parsers.py:** Allows parsing SCALE-UP output files.
- **handlers.py:** Manages FDF file settings and launches the simulations.
- **generators.py:** Classes to generate auxiliary files, such as the geometry ".restart" files.
- **structures.py:** Defines the data structures used in the other modules.
- **exceptions.py:** Declarations of the exceptions within the package.
- **files.py:** Classes for writing the output ".csv" files.

II Simulations in this Work

The code for the simulations carried out in this work is presented under the **examples** section, divided in strain-free and strain-fixed simulations.

The **main.py** files execute the simulations, which may be configured from the "User-defined Settings" section within the same file. They run the simulations, storing their data in a folder named **output**, and analyze it, producing basic graphs and data files that end up in two folders named **plots** and **csv** respectively.

Additionally, the **graph.py** scripts read the data files stored in **csv** to create the production-level figures displayed in Chapter **main.py** of this work. The **domains.py** produces the domain plots in the same chapter, but reads the information from the simulation **output** directly instead.

It must be noted that the strain-free simulations are split into three parts, as mentioned in Chapter 5, due to the increased supercell size used in the simulations near the AFD transition temperature.

BIBLIOGRAPHY

[1] N. W. Ashcroft and N. D. Mermin. *Solid State Physics*. Cengage Learning, 2011. URL https://books.google.es/books?id=x_s_YAAACAAJ.

[2] J. A. Bert, B. Kalisky, C. Bell, M. Kim, Y. Hikita, H. Y. Hwang, and K. A. Moler. Direct imaging of the coexistence of ferromagnetism and superconductivity at the LaAlO3/SrTiO3 interface. *Nature Physics*, 7(10):767–771, 10 2011. doi:10.1038/nphys2079.

[3] N. Bickel, G. Schmidt, K. Heinz, and K. Mller. Ferroelectric relaxation of the SrTiO3(100) surface. *Physical Review Letters*, 62(17):2009–2011, 4 1989. doi:10.1103/PhysRevLett.62.2009.

[4] E. Bousquet, M. Dawber, N. Stucki, C. Lichtensteiger, P. Hermet, S. Gariglio, J. M. Triscone, and P. Ghosez. Improper ferroelectricity in perovskite oxide artificial superlattices. *Nature*, 452(7188):732–736, 4 2008. doi:10.1038/nature06817.

[5] A. Bussmann-Holder, H. Büttner, and A. R. Bishop. Polar-soft-mode-driven structural phase transition in SrTiO3. *Physical Review Letters*, 99(16):167603, 10 2007. doi:10.1103/PhysRevLett.99.167603.

[6] P. Chandra and P. B. Littlewood. A Landau Primer for Ferroelectrics. *Topics in Applied Physics*, 105:69–116, 9 2006. URL http://arxiv.org/abs/cond-mat/0609347.

[7] P. Chen, M. N. Grisolia, H. J. Zhao, O. E. Gonzalez-Vazquez, L. Bellaiche, M. Bibes, B.-G. Liu, and J. Iniguez. Energetics of oxygen-octahedra rotations in perovskite oxides from first principles. *Physical Review B*, 97(2), 2 2018. doi:10.1103/PhysRevB.97.024113.

[8] W. Cochran. Crystal stability and the theory of ferroelectricity. *Physical Review Letters*, 3(9):412–414, 11 1959. doi:10.1103/PhysRevLett.3.412.

[9] C. J. Cramer. *Essentials of computational chemistry: theories and models*. Wiley, 2º edition, 2004.

[10] D. Damjanovic. Ferroelectric sensors. *IEEE Sensors Journal*, 1(3):191–206, 2001. doi:10.1109/JSEN.2001.954832.

[11] S. Das, Y. L. Tang, Z. Hong, M. A. Gonçalves, M. R. McCarter, C. Klewe, K. X. Nguyen, F. Gómez-Ortiz, P. Shafer, E. Arenholz, V. A. Stoica, S. L. Hsu, B. Wang, C. Ophus, J. F. Liu, C. T. Nelson, S. Saremi, B. Prasad, A. B. Mei, D. G. Schlom, J. Íñiguez, P. García-Fernández, D. A. Muller, L. Q. Chen, J. Junquera, L. W. Martin, and R. Ramesh. Observation of room-temperature polar skyrmions. *Nature*, 568(7752):368–372, 4 2019. doi:10.1038/s41586-019-1092-8.

[12] M. Elstner, D. Porezag, G. Jungnickel, J. Elsner, M. Haugk, and T. Frauenheim. Self-consistent-charge density-functional tight-binding method for simulations of complex materials properties. *Physical Review B - Condensed Matter and Materials Physics*, 58(11):7260–7268, 9 1998. doi:10.1103/PhysRevB.58.7260.

[13] L. Fang, L. You, and J.-M. Liu. Ferroelectrics in Photocatalysis. In *Ferroelectric Materials for Energy Applications*, pages 265–309. Wiley-VCH Verlag GmbH & Co. KGaA, Weinheim, Germany, 9 2018. doi:10.1002/9783527807505.ch9.

[14] P. Garcia-Fernandez, J. A. Aramburu, M. T. Barriuso, and M. Moreno. Key role of covalent bonding in octahedral tilting in perovskites. *Journal of Physical Chemistry Letters*, 1(3):647–651, 2 2010. doi:10.1021/jz900399m.

[15] P. García-Fernández, S. Ghosh, N. J. English, and J. A. Aramburu. Benchmark study for the application of density functional theory to the prediction of octahedral tilting in perovskites. *Physical Review B - Condensed Matter and Materials Physics*, 86(14):144107, 10 2012. doi:10.1103/PhysRevB.86.144107.

[16] P. García-Fernández, J. C. Wojdeł, J. Íñiguez, and J. Junquera. Second-principles method for materials simulations including electron and lattice degrees of freedom. *Physical Review B*, 93(19), 11 2016. doi:10.1103/PhysRevB.93.195137.

[17] M. R. Geller and W. Kohn. Theory of generalized Wannier functions for nearly periodic potentials. *Physical Review B*, 48(19):14085–14088, 11 1993. doi:10.1103/PhysRevB.48.14085.

[18] P. Ghosez. First-principles study of the dielectric and dynamical properties of barium titanate. 1997.

[19] A. M. Glazer. The classification of tilted octahedra in perovskites. *Acta Crystallographica Section B Structural Crystallography and Crystal Chemistry*, 28(11):3384–3392, 11 1972. doi:10.1107/s0567740872007976.

[20] A. M. Glazer. Simple ways of determining perovskite structures. *Acta Crystallographica Section A*, 31(6):756–762, 11 1975. doi:10.1107/S0567739475001635.

[21] V. M. Goldschmidt. Die Gesetze der Krystallochemie. *Die Naturwissenschaften*, 14(21):477–485, 5 1926. doi:10.1007/BF01507527.

[22] M. A. Gonçalves, C. Escorihuela-Sayalero, P. Garca-Fernández, J. Junquera, and J. Íñiguez. Theoretical guidelines to create and tune electric skyrmion bubbles. *Science Advances*, 5(2):eaau7023, 2 2019. doi:10.1126/sciadv.aau7023.

[23] X. Gonze, B. Amadon, and G. Antonius. The ABINITproject: Impact, environment and recent developments. *Computer Physics Communications*, 248:107042, 3 2020. doi:10.1016/j.cpc.2019.107042.

[24] T. Gu, T. Scarbrough, Y. Yang, J. Íñiguez, L. Bellaiche, and H. J. Xiang. Cooperative Couplings between Octahedral Rotations and Ferroelectricity in Perovskites and Related Materials. *Physical Review Letters*, 120(19):197602, 5 2018. doi:10.1103/PhysRevLett.120.197602.

[25] J. H. Haeni, P. Irvin, W. Chang, R. Uecker, P. Reiche, Y. L. Li, S. Choudhury, W. Tian, M. E. Hawley, B. Craigo, A. K. Tagantsev, X. Q. Pan, S. K. Streiffer, L. Q. Chen, S. W. Kirchoefer, J. Levy, and D. G. Schlom. Room-temperature ferroelectricity in strained SrTiO3. *Nature*, 430(7001):758–761, 8 2004. doi:10.1038/nature02773.

[26] D. R. Hartree. The Wave Mechanics of an Atom with a Non-Coulomb Central Field Part II Some Results and Discussion. *Mathematical Proceedings of the Cambridge Philosophical Society*, 24(1):111–132, 1928. doi:10.1017/S0305004100011920.

[27] J. C. W. P. Hermet, M. P. Ljungberg, P. Ghosez, and J. Íñiguez. First-principles model potentials for lattice-dynamical studies: general methodology and example of application to ferroic perovskite oxides. *Journal of Physics: Condensed Matter*, 25(30):305401, 7 2013. doi:10.1088/0953-8984/25/30/305401.

[28] P. Hohenberg and W. Kohn. Inhomogeneous electron gas. *Physical Review*, 136(3B):B864, 11 1964. doi:10.1103/PhysRev.136.B864.

[29] C. J. Howard and H. T. Stokes. Group-Theoretical Analysis of Octahedral Tilting in Perovskites. *Acta Crystallographica Section B: Structural Science*, 54(6):782–789, 12 1998. doi:10.1107/S0108768198004200.

[30] M. Itoh and R. Wang. Quantum ferroelectricity in SrTiO3 induced by oxygen isotope exchange. *Applied Physics Letters*, 76(2):221–223, 1 2000. doi:10.1063/1.125708.

[31] H. W. Jang, A. Kumar, S. Denev, M. D. Biegalski, P. Maksymovych, C. W. Bark, C. T. Nelson, C. M. Folkman, S. H. Baek, N. Balke, C. M. Brooks, D. A. Tenne, D. G. Schlom, L. Q. Chen, X. Q. Pan, S. V. Kalinin, V. Gopalan, and C. B. Eom. Ferroelectricity in strain-free SrTiO3 thin films. *Physical Review Letters*, 104(19):197601, 5 2010. doi:10.1103/PhysRevLett.104.197601.

[32] F. Jensen. *Introduction to Computational Chemistry*. Wiley, 2 edition, 2007. URL https://books.google.es/books?id=RDIG48UcZfYC.

[33] J. Junquera and P. Ghosez. Critical thickness for ferroelectricity in perovskite ultrathin films. *Nature*, 422(6931):506–509, 4 2003. doi:10.1038/nature01501.

[34] A. Kakekhani, S. Ismail-Beigi, and E. I. Altman. Ferroelectrics: A pathway to switchable surface chemistry and catalysis. *Surface Science*, 650:302–316, 8 2016. doi:10.1016/j.susc.2015.10.055.

[35] J. Kiat and T. Roisnel. Rietveld analysis of strontium titanate in the Müller state. *Journal of Physics: Condensed Matter*, 8(19):3471–3475, 1996. doi:10.1088/0953-8984/8/19/021.

[36] C. Kittel. *Introduction to Solid State Physics*. 8 edition, 2004.

[37] W. Kohn and L. J. Sham. Self-consistent equations including exchange and correlation effects. *Physical Review*, 140(4A):A1133, 11 1965. doi:10.1103/PhysRev.140.A1133.

[38] B. Koslowski, R. Notz, and P. Ziemann. Epitaxial growth of iridium on strontium-titanate (0 0 1) studied by in situ scanning tunneling microscopy. *Surface Science*, 496(3):153–159, 1 2002. doi:10.1016/S0039-6028(01)01631-4.

[39] D. P. Landau and K. Binder. *A Guide to Monte Carlo Simulations in Statistical Physics*. Cambridge University Press, 2014. doi:10.1017/cbo9781139696463.

[40] L. Landau. *Collected Papers of L.D. Landau*. Elsevier, 1965. doi:10.1016/c2013-0-01806-3.

[41] A. W. Leissa. The historical bases of the Rayleigh and Ritz methods. *Journal of Sound and Vibration*, 287(4-5):961–978, 11 2005. doi:10.1016/j.jsv.2004.12.021.

[42] S. B. Levin, N. J. Field, F. M. Plock, and L. Merker. Some Optical Properties of Strontium Titanate Crystal. *Journal of the Optical Society of America*, 45(9):737, 9 1955. doi:10.1364/josa.45.000737.

[43] X. Li, T. Qiu, J. Zhang, E. Baldini, J. Lu, A. M. Rappe, and K. A. Nelson. Terahertz field–induced ferroelectricity in quantum paraelectric SrTiO3. *Science*, 364(6445):1079–1082, 6 2019. doi:10.1126/science.aaw4913.

[44] C.-H. Lin, C.-M. Huang, and G. Y. Guo. Systematic ab initio study of the phase diagram of epitaxially strained SrTiO3. *Journal of Applied Physics*, 100(8), 7 2006. doi:10.1063/1.2358305.

[45] E. L. Lin, B. I. Edmondson, S. Hu, and J. G. Ekerdt. Epitaxial growth of perovskite strontium titanate on germanium via atomic layer deposition. *Journal of Visualized Experiments*, 2016(113), 7 2016. doi:10.3791/54268.

[46] M. Łopuszyński and J. A. Majewski. Ordering in ternary nitride semiconducting alloys. *Physical Review B - Condensed Matter and Materials Physics*, 85(3), 1 2012. doi:10.1103/PhysRevB.85.035211.

[47] W. Mckinney. Data Structures for Statistical Computing in Python. Technical report, 2010.

[48] H. D. Megaw. *Crystal structures: a working approach*. Saunders, 1973.

[49] N. Metropolis and S. Ulam. The Monte Carlo Method. *Journal of the American Statistical Association*, 44(247):335, 9 1949. doi:10.2307/2280232.

[50] K. Momma and F. Izumi. VESTA 3 for three-dimensional visualization of crystal, volumetric and morphology data. *Journal of Applied Crystallography*, 44(6):1272–1276, 12 2011. doi:10.1107/S0021889811038970.

[51] K. A. Müller and H. Burkard. SrTiO3: An intrinsic quantum paraelectric below 4 K. *Physical Review B*, 19(7):3593–3602, 1979. doi:10.1103/PhysRevB.19.3593.

[52] K. Munakata and A. Okazaki. Ultra-high-angle double-crystal X-ray diffractometry (U-HADOX) for determining a change in the lattice spacing: Experiment. *Acta Crystallographica Section A: Foundations of Crystallography*, 60(1):33–39, 1 2004. doi:10.1107/S0108767303022633.

[53] A. Ohtomo and H. Y. Hwang. A high-mobility electron gas at the LaAlO3/SrtiO3 heterointerface. *Nature*, 427(6973):423–426, 1 2004. doi:10.1038/nature02308.

[54] R. G. Parr and W. Yang. *Density-functional theory of atoms and molecules*. Oxford University Press, 1989.

[55] J. Pérez-Ramírez and B. Vigeland. Perovskite Membranes in Ammonia Oxidation: Towards Process Intensification in Nitric Acid Manufacture. *Angewandte Chemie International Edition*, 44(7):1112–1115, 2 2005. doi:10.1002/anie.200462024.

[56] N. Pertsev, A. Tagantsev, and N. Setter. Phase transitions and strain-induced ferroelectricity in epitaxial thin films. *Physical Review B - Condensed Matter and Materials Physics*, 61(2):R825–R829, 2000. doi:10.1103/PhysRevB.61.R825.

[57] B. L. Phoon, C. W. Lai, J. C. Juan, P. L. Show, and G. T. Pan. Recent developments of strontium titanate for photocatalytic water splitting application. *International Journal of Hydrogen Energy*, 44(28):14316–14340, 5 2019. doi:10.1016/j.ijhydene.2019.01.166.

[58] R. Ramesh and N. A. Spaldin. Multiferroics: Progress and prospects in thin films, 1 2007. doi:10.1038/nmat1805.

[59] G. K. Ray. Some studies on phonon scattering in solids. *Calcutta University*, 1980.

[60] C. C. Roothaan. New developments in molecular orbital theory. *Reviews of Modern Physics*, 23(2):69–89, 4 1951. doi:10.1103/RevModPhys.23.69.

[61] N. Sai and D. Vanderbilt. First-principles study of ferroelectric and antiferrodistortive instabilities in tetragonal SrTiO3. *Physical Review B - Condensed Matter and Materials Physics*, 62(21):13942–13950, 4 2000. doi:10.1103/PhysRevB.62.13942.

[62] A. Schiaffino and M. Stengel. Macroscopic Polarization from Antiferrodistortive Cycloids in Ferroelastic SrTiO3. *Physical Review Letters*, 119(13):137601, 9 2017. doi:10.1103/PhysRevLett.119.137601.

[63] J. F. J. F. Scott. *Ferroelectric memories*. Springer, 2000.

[64] W. Setyawan and S. Curtarolo. High-throughput electronic band structure calculations: Challenges and tools. *Computational Materials Science*, 49(2):299–312, 8 2010. doi:10.1016/j.commatsci.2010.05.010.

[65] R. D. Shannon. Revised effective ionic radii and systematic studies of interatomic distances in halides and chalcogenides. *Acta Crystallographica Section A*, 32(5):751–767, 9 1976. doi:10.1107/S0567739476001551.

[66] J. C. Slater. Note on hartree's method, 1 1930. doi:10.1103/PhysRev.35.210.2.

[67] I. Souza, N. Marzari, and D. Vanderbilt. Maximally localized Wannier functions for entangled energy bands. *Physical Review B - Condensed Matter and Materials Physics*, 65(3):1–13, 12 2002. doi:10.1103/PhysRevB.65.035109.

[68] J. Sun, T. Gao, X. Song, Y. Zhao, Y. Lin, H. Wang, D. Ma, Y. Chen, W. Xiang, J. Wang, Y. Zhang, and Z. Liu. Direct growth of high-quality graphene on high-k dielectric SrTiO 3 substrates. *Journal of the American Chemical Society*, 136(18):6574–6577, 5 2014. doi:10.1021/ja5022602.

[69] S. Thomas and A. Thankappan. *Perovskite photovoltaics: Basic to advanced concepts and implementation*. Elsevier, 1 2018. doi:10.1016/C2016-0-03790-7.

[70] A. Tkach and P. M. Vilarinho. *Strontium Titanate : Synthesis, Properties and Uses*. Nova Science Publishers, 2019.

[71] J. J. Urban, W. S. Yun, Q. Gu, and H. Park. Synthesis of single-crystalline perovskite nanorods composed of barium titanate and strontium titanate. *Journal of the American Chemical Society*, 124(7):1186–1187, 2 2002. doi:10.1021/ja017694b.

[72] S. van der Walt, S. C. Colbert, and G. Varoquaux. The NumPy Array: A Structure for Efficient Numerical Computation. *Computing in Science Engineering*, 13(2):22–30, 2011. doi:10.1109/MCSE.2011.37.

[73] H. E. Weaver. Dielectric properties of single crystals of SrTiO3 at low temperatures. *Journal of Physics and Chemistry of Solids*, 11(3-4):274–277, 10 1959. doi:10.1016/0022-3697(59)90226-4.

[74] P. M. Woodward. Octahedral Tilting in Perovskites. I. Geometrical Considerations. *Acta Crystallographica Section B: Structural Science*, 53(1):32–43, 2 1997. doi:10.1107/S0108768196010713.

[75] P. M. Woodward. Octahedral Tilting in Perovskites. II. Structure Stabilizing Forces. *Acta Crystallographica Section B: Structural Science*, 53(1):44–66, 2 1997. doi:10.1107/S0108768196012050.

[76] Y. Zhang, L. Zhong, and D. Duan. Single-step hydrothermal synthesis of strontium titanate nanoparticles from crystalline anatase titanium dioxide. *Ceramics International*, 41(10):13516–13524, 12 2015. doi:10.1016/j.ceramint.2015.07.145.

[77] W. Zhong and D. Vanderbilt. Effect of quantum fluctuations on structural phase transitions in SrTiO3 and BaTiO3. *Physical Review B - Condensed Matter and Materials Physics*, 53(9):5047–5050, 3 1996. doi:10.1103/PhysRevB.53.5047.